JOURNAL OF FUEL CHEMISTRY AND TECHNOLOGY
Volume 54, Issue 8, August 2026

燃料化学学报(中英文)
Journal of Fuel Chemistry and Technology

Cite this article as: J Fuel Chem Technol, 2026, 54, 20250325

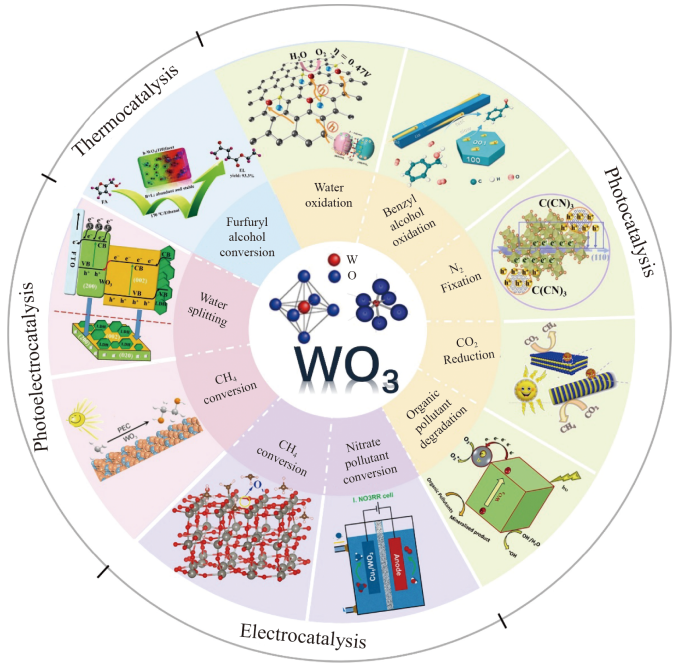
REVIEW

Crystal facet effect of WO_3 in heterogeneous catalysis

ZHANG Miao[1], WANG Huixiang[1,2,*], LI Huipeng[2,3], ZHANG Deshun[2,3], XU Jingwen[1], REN Duojia[1], ZHANG Wei[1], XUE Shoufeng[1], LÜ Baoliang[1,2,*]

[1] School of Chemistry and Chemical Engineering, Shanxi Normal University, Taiyuan 030031, China;
[2] Shanxi Key Laboratory of Coal-based Synthetic Oil Product Testing, Changzhi 046000, China;
[3] Shanxi Lu'an Coal-based Clean Energy Limited Liability Company, Changzhi 046200, China

Abstract: As an important transition metal oxide, tungsten trioxide (WO_3) has become one of the most attractive materials in the current field of heterogeneous catalysis due to its comprehensive merits in environmental friendliness, cost-effectiveness and electrical properties. Different crystal facets of WO_3 exhibit significant differences in key catalytic physicochemical properties such as charge separation efficiency, reactant adsorption capacity, and redox activity, which stems from the inherent differences in their atomic arrangement, electronic structure, and surface energy. Relevant studies have confirmed that, influenced by the distinct facet effect, the catalytic performance of WO_3 strongly depends on the exposed facet states determined by its geometric morphology. This finding provides an important direction for mechanism research of modern heterogeneous catalysis. This paper reviews the facet effect of WO_3 as a heterogeneous catalyst in various application fields in recent years, including photocatalysis, electrocatalysis, photoelectrocatalysis, and thermal catalysis process. Meanwhile, combined with theoretical calculations, it explains the intrinsic mechanism underlying the facet effect from the perspective of the atomic structure essence of WO_3 crystal facets. Finally, the paper summarizes the general rules of the WO_3 facet effect across the aforementioned application scenarios, deeply discusses the shortcomings in the current research on the facet effect of WO_3, and prospects the future development direction of this field.



Key words: WO_3; crystal facet effect; heterogeneous catalysis

Catalysis plays a vital role in the fields of industrial production, energy conversion and environmental protection[1−5], such as petroleum refining[6], synthesis of fiber, plastic[7], clean utilization of coal[8] and exhaust gas denitrification[9]. Therefore, catalysis has evolved into a central discipline in chemistry, and in catalytic processes, heterogeneous catalysis is a core technology due to its advantages of easy separation and recovery, and suitability for continuous production[10].

The performance of a heterogeneous catalyst largely

Received: 2025-10-30; Revised: 2025-12-15
Foundation items: Supported by the Central Government's Special Fund for Local Science and Technology Development (YDZJSX20231A051), the Joint Funding Project of Shanxi Fundamental Research Program (Lu'an) (202403011241006), the National Natural Science Foundation of China (22505146), the Natural Science Foundation of Shanxi Province (202303021222189), the Outstanding Doctoral Research funding of Shanxi Province (020120240015), the Natural Science Foundation of Shanxi Normal University (JCYJ2023020, JCYJ2023011).
* Corresponding author. Tel: 0351-2051-294, E-mail: wanghx@sxnu.edu.cn, lvbl@sxnu.edu.cn.
DOI: 10.1016/S1872-5813(26)60684-6 CSTR: 32157.14.2097-213X.2026.JFCT.0041
本文的英文电子版由 Elsevier 出版社在 ScienceDirect 上出版 (http://www.sciencedirect.com/science/journal/18725813)

depends on its specific surface area. Therefore, researches on heterogeneous catalysis commonly adopt strategies such as constructing porous structures (e.g., materials with micropores, mesopores and even macropores), fabricating nanomaterials (e.g., nanoparticles, nanowires, nanosheets, nanoflowers), and engineering hierarchical structures (e.g., complex morphologies including core-shell, hollow, urchin-like and flower-like ones) to boost the specific surface area of heterogeneous catalysts. However, the irregularity and complexity of the aforementioned structures hinder the elucidation of reaction mechanisms at the molecular level and restrict the targeted design of catalysts with high activity, selectivity, and stability.

Since the mid-1950s, metal oxide catalysts have demonstrated irreplaceable roles in areas such as petroleum chemical processing, specialty chemicals synthesis, and environmental remediation, owing to their unique electronic structures and surface chemical properties[11]. Notably, the catalytic performance of these materials is not only correlated with chemical composition and crystal size, but also strongly associated with crystal morphology[12−13]. Specifically, by tailoring the morphology of catalysts to achieve selective exposure of specific crystal facets can significantly optimize their catalytic performance[14−15]. The underlying reason lies in the anisotropic nature of different crystals. Different crystal facets exhibit inherent differences in atomic arrangement, electronic structure and surface energy, which directly influence key catalytic properties such as reactant adsorption, charge separation, and redox activity[16−17]. This facet-dependent catalytic behavior provides a novel perspective for heterogeneous catalysis research and has made morphology-controlled nanocrystals a focal point of interest in the field of catalytic materials[18].

WO_3 is an outstanding *n*-type semiconductor metal oxide, with a high melting point, high strength, and excellent chemical stability[19−21]. It is not only extensively used in industrial scenarios such as high-melting-point alloys[22], hard alloys[23], fire-resistant materials[24], shielding materials[25], and ceramic colorants[26], but has also been practically applied in energy and sensing fields, including lithium-ion batteries, gas sensors, and supercapacitors[27]. Moreover, WO_3 has a visible-light-responsive bandgap of E_g (2.4–2.8 eV) and a high oxidation potential (>2.5 eV), so it also exhibits significant application value in photocatalysis and electrocatalysis[28]. Meanwhile, WO_3 features a high oxidation state and excellent thermal stability, thus exhibiting outstanding performance in thermocatalysis.

Over the past two decades, researchers have achieved groundbreaking progress in the study of WO_3 morphology control and facet effect in catalysis, and successfully synthesized WO_3 nanomaterials with exposed specific facets using multiple synthesis strategies, including vapor-phase, liquid-phase, and solid-phase methods[29−31]. For instance, Zheng et al.[32] prepared WO_3 thin film dominated by (002) facet on fluorine-doped tin oxide (FTO) glass substrates; Using a hydrothermal method with sodium tungstate as the tungsten source and acetic acid for pH adjustment, Li's team[28] synthesized WO_3 nanosheets and nanowires that exposed the (001) and (110) facet, respectively; Lee et al.[33] prepared WO_3 nanorods exposing the (001) facet using ammonium tungstate, while WO_3 nanorods exposing the (100) and (010) facets were synthesized with sodium tungstate as precursor. These studies have laid a solid material foundation for the systematic investigation of the facet effect of WO_3. Nevertheless, there remains a lack of systematic summaries regarding the structure-activity relationships, underlying mechanisms, and universal laws of the facet effect of WO_3 in diverse heterogeneous catalytic systems. Additionally, related research still confronts numerous scientific challenges and technical bottlenecks.

Against this backdrop, this review aims to systematically summarize the research advances in the facet effects of WO_3 catalysts in heterogeneous catalytic systems (e.g., photocatalysis, electrocatalysis, photoelectrocatalysis and thermal catalysis). Specifically, it focuses on the following aspects: (1) analyzing the structure-activity relationships of different WO_3 facets in various catalytic reactions; (2) elucidating the physicochemical mechanisms underlying the facet effect of distinct crystal facets; (3) summarizing the universal laws governing the facet effect of WO_3 in diverse catalytic systems; (4) discussing the key scientific issues and technical bottlenecks in current research on the WO_3 facet effect; (5) proposing potential breakthrough directions and innovative ideas for future studies in this field. In addition, a brief introduction is also given to the facet effect in the WO_3 sensing process. It is anticipated that this work will provide theoretical support for the rational design and performance optimization for WO_3-based catalytic materials, and offer new perspectives for the expanded application of facet engineering in the field of heterogeneous catalysis.

1 Facet effect of WO_3 in photocatalytic reactions

WO_3, as a non-toxic, earth-abundant, and low-cost semiconductor, possesses excellent chemical and thermal stability, tunable band gap, high electron mobility, and remarkable visible-light absorption capacity[34]. These properties make it an ideal candidate material in the field of semiconductor photocatalysis, exhibiting great application potential in scenarios such as photocatalytic water splitting for hydrogen production and pollutant degradation[35].

Currently, photocatalytic technology has attracted extensive research interest due to its ability to convert solar energy into chemical energy. However, photocatalysts generally suffer from issues like low light utilization efficiency and easy recombination of electron-hole (e^--h^+) pairs[36]. Crystal facet engineering by regulating the type and ratio of exposed crystal facets of nanomaterials can modify their band structures and atomic arrangements, thereby

effectively enhancing photocatalytic performance. Nevertheless, the specific mechanism by which the crystal facets of WO_3 regulate photocatalytic activity remains unclear. In the following sections, the photocatalytic performance and crystal facet effect of WO_3 will be discussed in detail in combination with specific catalytic reactions.

1.1 Water oxidation

Solar-driven water oxidation is an artificial photosynthesis method for clean energy production and storage[37]. In the study on the Cu_2O/WO_3 series of catalysts, Gong et al.[38] found that the loading method of Cu_2O over WO_3 exerted a crucial influence on the catalytic performance. Specifically, when the ascorbic acid liquid-phase reduction method was adopted, Cu_2O can be selectively loaded onto the edged (200) and (020) crystal facets of square-like WO_3 (as shown in Figure 1(a), (b)). While when the sodium borohydride liquid-phase reduction method was used, it was randomly distributed on the predominant (002) crystal facet (as shown in Figure 1 (c), (d)). After Pt was loaded onto these two catalysts (named $Pt@Cu_2O/WO_3$ and Cu_2O-Pt/WO_3 for the former and latter, respectively), Figure 1(e) shows the photocatalytic activity under different Cu_2O loadings of the composite catalyst.

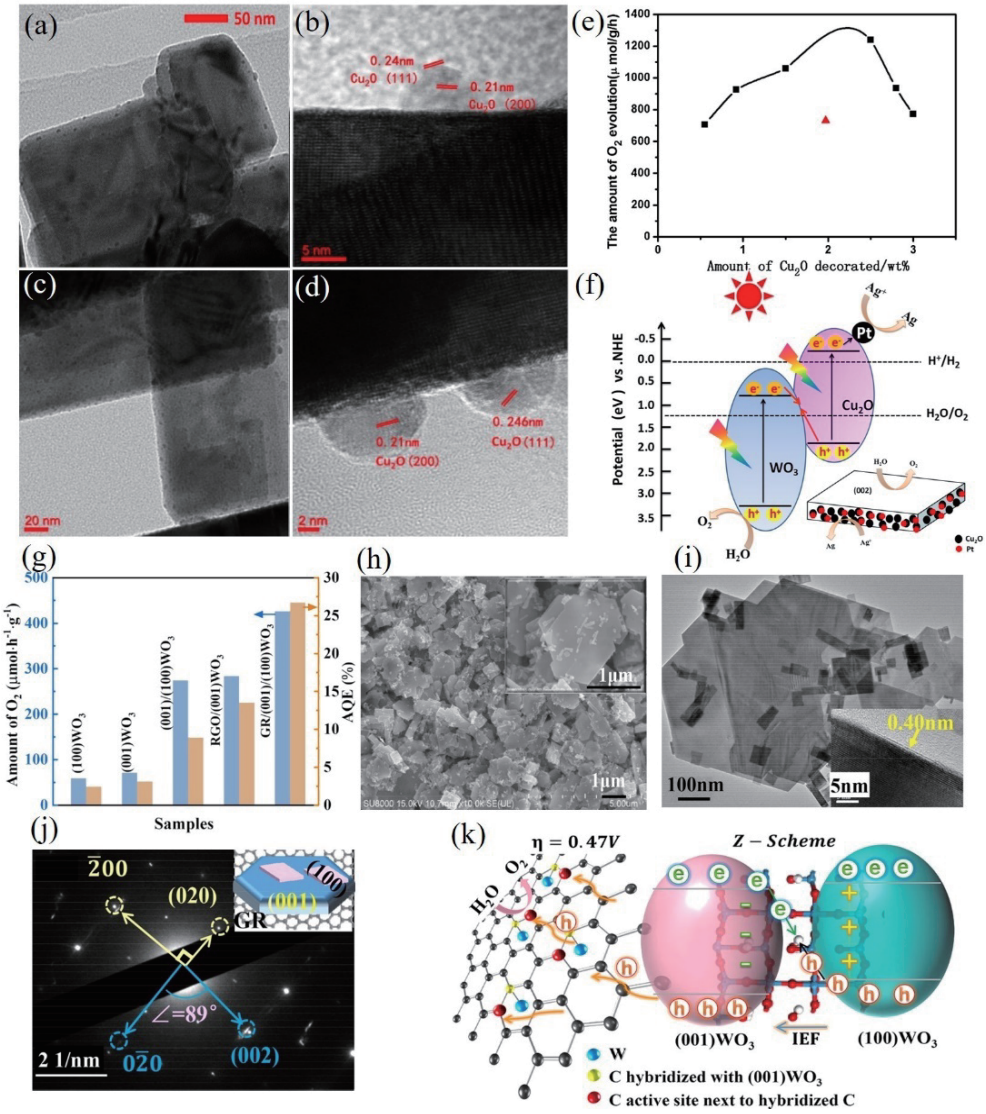


Fig. 1 (a) TEM and (b) HRTEM images of Cu_2O/WO_3 prepared by ascorbic acid liquid-phase reduction method; (c) TEM and (d) HRTEM images of Cu_2O/WO_3 prepared by sodium borohydride liquid phase reduction; (e) Photocatalytic water oxidation activities of different Cu_2O loadings; (f) Schematic diagram for photoexcited carriers separation processes in $Pt@Cu_2O/WO_3$ photocatalyst; (g) The rate of O_2 production and AQE (apparent quantum efficiency) on (100) and (001) planes of WO_3; (h) SEM, (i) TEM images and (j) SAED pattern of GR/(001)/(100)WO_3 (its schematic diagram is inset of (j)); (k) The possible mechanism for the enhanced water oxidation on this unique catalyst[38−39]
(with permission from Elsevier)

At a loading of 1.97%, the photocatalytic O_2 evolution rate of Cu_2O-Pt/WO_3 is only 731.9 μmol/(g·h) (red solid triangle), which is much lower than that of Pt@Cu_2O/WO_3 (1238.6 μmol/(g·h)). The reaction mechanism was proposed as follows. On one hand, square-like WO_3 itself exhibited spatial separation of photogenerated charges between different crystal facets: photogenerated holes (h^+) tended to migrate preferentially to the (002) facet to form a h^+-rich region, while photogenerated electrons (e^-) accumulated on the edge of (200) and (020) facets to form an e^--rich region, participating in the photooxidation and photoreduction half-reactions respectively. On the other hand, the catalyst followed the Z-scheme charge transfer mechanism: after WO_3 and Cu_2O were photoexcited, the photogenerated e^- in the conduction band (CB) of WO_3 migrated to the edge of (200) and (020) facets and recombined with the photogenerated h^+ in the valence band (VB) of Cu_2O at the interface. This process not only retained the h^+ with strong oxidizing ability in the VB of WO_3 but also preserved the e^- with strong reducing ability in the CB of Cu_2O. Meanwhile, Pt can efficiently capture the e^- from Cu_2O and transfer them to $AgNO_3$ (serving as the sacrificial agent) to reduce Ag^+ to Ag. It is precisely the synergy of these effects that significantly improves the catalytic efficiency, enabling Pt@Cu_2O/WO_3 to exhibit excellent photocatalytic O_2 evolution performance (Figure 1(f)).

Wang et al.[39] designed an unique graphene (GR) hybridized 2D ternary GR/(001)/(100)WO_3 facet junction *via* a graphene hybridization strategy, which further confirmed the intrinsic difference in the photocatalytic activity of WO_3 with different exposed facets. As shown in Figure 1(g), the photocatalytic oxidation activity of WO_3 with exposed (001) facets was higher compared with that exposed (100) facets. The core design of this catalyst centers on the combination of the advantages of specific crystal facets and the functional properties of graphene: through a facile two-step hydrothermal method, WO_3 with highly exposed (001) facets (denoted as (001) WO_3) was first tightly connected to GR *via* -C-W- "bridges". Figure 1 (h), (i) showed the corresponding micromorphology, and a proposed sandwich-like configuration was illustrated in Figure 1(j). Graphene, with its dual functions as a "h^+ trap" and a "co-catalyst", not only efficiently captured photo-generated h^+ to reduce charge recombination but also accelerated reaction kinetics. Subsequently, WO_3 with (100) facets (denoted as (100) WO_3) were grown epitaxially on the surface of (001) WO_3, constructing a multi-facet synergistic composite structure (Figure 1(k)). Eventually, the GR/(001)/(100) WO_3 facet junction exhibited excellent water oxidation performance, achieving an apparent quantum efficiency of 26% at 420 nm. The intrinsic origin of its performance advantage lied in the full utilization of the high oxidation activity of the (001) facets of WO_3, as well as the efficient charge transfer and reaction system synergistically constructed by graphene and the facet junction.

1.2 Oxidation of benzyl alcohol

Using clean, renewable solar energy instead of traditional fossil fuels to drive reactions enables efficient conversion of benzyl alcohol into high-value-added chemicals, providing core technical support for green upgrading in the fine chemical industry[40−41]. Li's research group[28] systematically investigated the photocatalytic performance of WO_3 nanowires with exposed (110) facet and WO_3 nanosheets with exposed (001) facet in the selective oxidation of benzyl alcohol to benzaldehyde (Figure 2 (a)−(d)). Experimental results demonstrated that the activity of WO_3 with (110) facets for benzyl alcohol oxidation is 2.46 times than that of WO_3 with (001) facets (0.11 mmol/(g·h)).

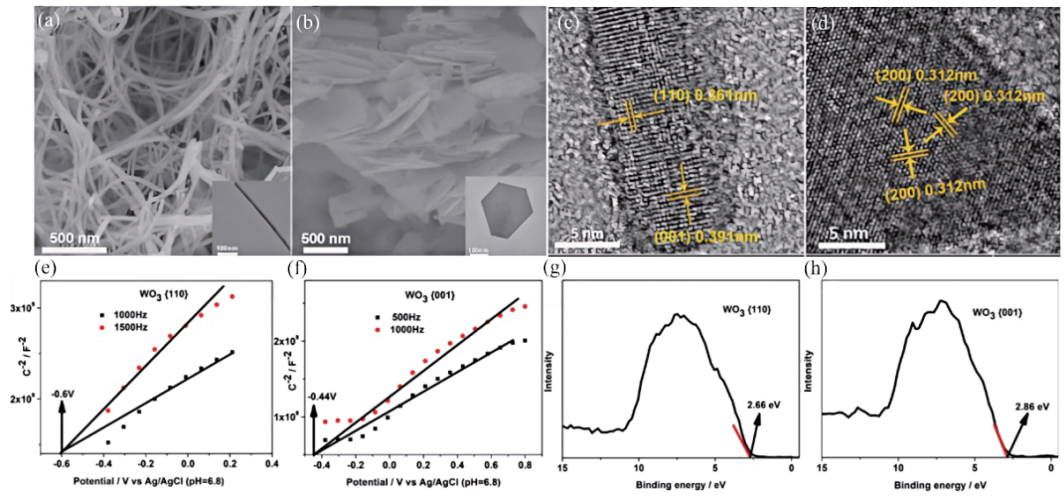


Fig. 2 (a) and (b) SEM graph of nanowire and nanosheet (inset TEM graph); (c) and (d) HRTEM graph of nanowire and nanosheet; (e), (f) Mott-Schottky plot of (110) and (001); (g), (h) XPS valence band spectrum of (110) and (001)[28] (with permission from ACS Publications)

To elucidate the underlying mechanism, density functional theory (DFT) calculations were performed, which revealed that the effective mass of photogenerated h^+ on the (110) facet (0.94 m_0, where m_0 denotes the rest mass of an electron) is significantly lower than that on the (001) facet (1.28 m_0). This difference in h^+ effective mass directly leads to a distinction in h^+ mobility between the two facets: the (110) facet exhibits a higher h^+ mobility of 4.92 $cm^2/(V·s)$, whereas the (001) facet shows a lower value of 3.14 $cm^2/(V·s)$. Further calculations based on the Einstein equation and h^+ lifetime data indicate that the h^+ diffusion length on the (110) facet (74.8 nm) is longer than that on the (001) facet (53.4 nm).

In conclusion, the superior photocatalytic performance of the (110) facet arises from the synergistic effects of h^+: lower effective mass, higher mobility, and longer diffusion length. Meanwhile, Mott-Schottky measurements and XPS (X-ray Photoelectron Spectroscopy) valence band spectrum elucidate the carrier differences between various crystal facets based on microscopic physical mechanisms (Figure 2 (e)−(h)).

1.3 N_2 fixation

Photocatalytic N_2 fixation technology utilizes clean and renewable solar energy as the energy source, featuring mild reaction conditions and environmental friendliness. Replacing the conventional NH_3 production process (Haber-Bosch process) holds great significance for energy utilization and environmental sustainability[42−43]. Currently, the commonly used catalysts mainly include metal oxides, bismuth oxyhalides, and graphitic carbon nitride[44]. However, the photoexcited e^- on these catalysts tend to recombine with h^+, making it difficult to activate the stable N≡N triple bond, and the electron accumulation efficiency remains low. Restricted by these issues, the efficiency of existing systems is far from meeting practical application requirements[45].

To overcome this bottleneck, Xiong et al.[46] pioneered a unique strategy of "electron pump-enhanced facet engineering". By synergistically tailoring crystal facets and co-catalysts, they constructed a WO_3/$C(CN)_3$ composite photocatalytic system for N_2 fixation. This system employed WO_3 nanosheets (WO_3 NS) with exposed (100) facet and WO_3 nanowires (WO_3 NW) with exposed (110) facet as substrates, which were coupled with a novel organic semimetallic cocatalyst $C(CN)_3$. The core design concept is to regulate the interfacial charge transfer pathway by leveraging the differences in electronic structures between different facets of WO_3. As shown in Figure 3(a), HRTEM image revealed that the predominantly exposed facet of WO_3 NS is the (100) facet, on which $C(CN)_3$ was preferentially coated, while WO_3 NW interacted with $C(CN)_3$ *via* the (110) facet.

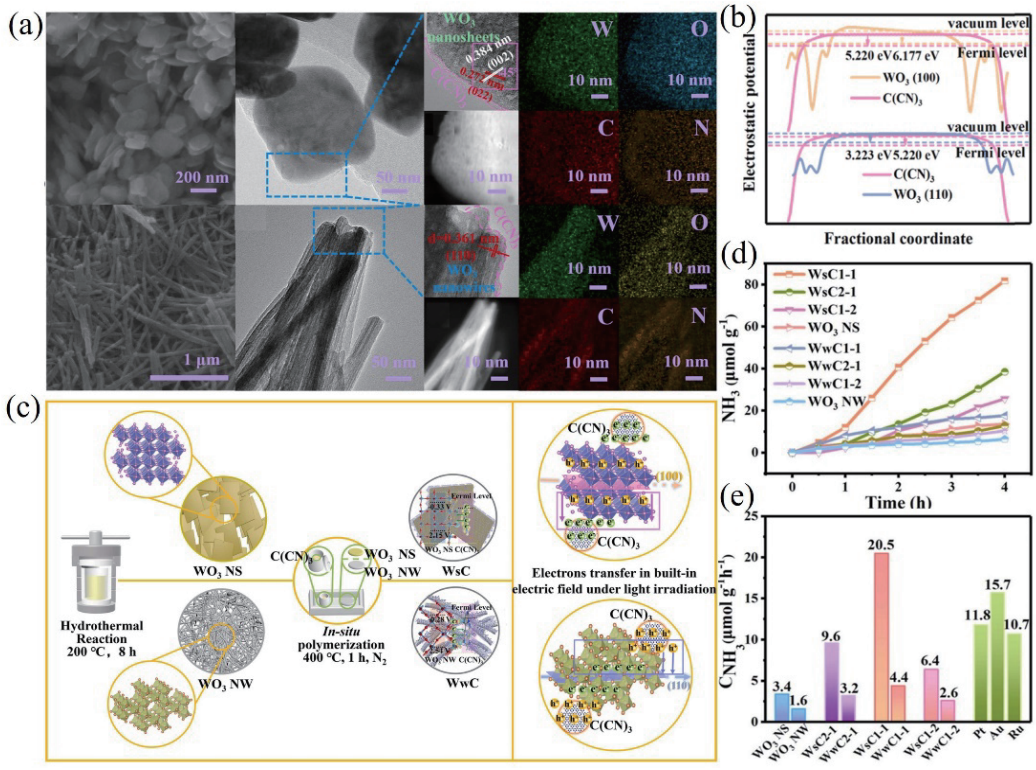


Fig. 3 (a) FE-SEM, TEM, HRTEM, HAADF and EDS mapping images of WsC1-1 and WwC1-1; (b) Electrostatic potential of $C(CN)_3$, WO_3 NS (100) and WO_3 NW (110); (c) Synthesis of WsC and WwC composites, and the electrons transfer in built-in electric field under light irradiation; (d) NH_3 yield of the prepared samples (λ > 420 nm); (e) The production rate of NH_3 of the prepared samples[46]
(with permission from Elsevier)

The calculated work functions of W_f (WO_3 NS: 6.177 eV, WO_3 NW: 3.223 eV, $C(CN)_3$: 5.220 eV) provided a theoretical basis for determining the direction of electron transfer (Figure 3(b)). Combined with the effect of the interfacial built-in electric field, the charge transfer behaviors of the two composite systems were finally clarified. In the WO_3 NS/$C(CN)_3$ system (WsC), the built-in electric field drives photogenerated e^- to be directionally "pumped" from the (100) facet of WO_3 into the active sites of $C(CN)_3$, rendering $C(CN)_3$ e^--enriched and thus enabling efficient activation of N_2; In the WO_3 NW/$C(CN)_3$ system (WwC), the reversed direction of the built-in electric field leads to electron transfer from $C(CN)_3$ to the (110) facet of WO_3, resulting in $C(CN)_3$ becoming electron-deficient and losing its N_2 fixation activity (Figure 3(c)). The results of performance tests further confirm the effectiveness of this strategy. As shown in Figure 3(d), (e), the NH_3 production of pure WO_3 NS and WO_3 NW is relatively low, reaching only 3.4 and 1.6 μmol/(g·h), respectively. After modification with $C(CN)_3$, the catalytic activity of the WsC composites is significantly enhanced. Among them, the WsC1-1 sample (WsC1-1 represents the ratio of WO_3 NS to $C(CN)_3$ of 1∶1) achieves an NH_3 production of 20.475 μmol/(g·h), which is 4.7 times that of the WwC.

1.4 CO_2 reduction

Solar-driven reduction of CO_2 to high-value hydrocarbon fuels and CO is recognized as an effective approach to address global warming and energy crisis[47−48]. Among various tungsten oxides, WO_3 is widely employed in the photocatalytic reduction of CO_2 due to its facile preparation and excellent controllability over structure and morphology[49].

Xie et al.[50] successfully synthesized two types of WO_3 crystals by controlling the acid hydrolysis of crystalline WB: quasi-cubic WO_3 with nearly equal proportions of (002), (200) and (020) facets, and rectangular sheet-like WO_3 dominated by (002) facets. Figure 4(a) showed the atomic structure models of the (002), (020) and (200) facets in monoclinic WO_3. When these two WO_3 samples were used for the photocatalytic reduction of CO_2 to CH_4 under the same conditions and a significant difference in performance was observed: the WO_3 nanosheets predominantly exposing (002) facets exhibited an activity of 0.34 μmol/(g·h), while the quasi-cubic WO_3 showed no activity. This result indicated that the (002) facet of WO_3 servers as the key active facet for CO_2 photoreduction.

Zhang et al.[51] integrated facet engineering with heterojunction construction. They prepared 1D WO_3 nanowires dominated by (110) facets (WO_3-110) and 2D hexagonal WO_3 nanosheets dominated by (001) facets (WO_3-001) *via* a hydrothermal method (as shown in Figure 4 (b)−(f)) and further coupled these two WO_3 samples with CuO nanoparticles respectively to construct *p-n* heterojunction photocatalysts for CO_2 photoreduction. To compare and analyze the separation-recombination performance of photogenerated e^--h^+ pairs between CuO-WO_3-001 nanosheets and CuO-WO_3-110 nanowires, the measurements of photocurrent, electrochemical impedance spectroscopy (EIS), and photoluminescence (PL) were employed (as shown in Figure 4(h)−(j)). All three methods consistently demonstrate that the CuO-WO_3-110 nanowires outperformed the CuO-WO_3-001 nanosheets in both the separation efficiency of e^--h^+ pairs and the interfacial charge transfer rate (Figure 4(g)). Owing to the fact that the (110) facet is more conductive to charge carrier migration, WO_3-110 exhibited higher activity than WO_3-001, the CO yield of the WO_3-110/CuO composite reached 7.647 μmol/(g·h).

Shi et al.[52] focused on the activity optimization of the WO_3(001) facet in heterojunction systems. Using FTO as the substrate, they synthesized two types of Cu_2O-modified hexagonal WO_3 nanosheet catalysts *via* vertical growth: Cu_2O/WO_3-001 (with dominant (001) facets) and Cu_2O/WO_3 (without dominant (001) facets). The photocatalytic CO_2 reduction activities of the two catalysts were evaluated under visible light irradiation. The results showed that the activity of Cu_2O/WO_3-001 was superior to that of pure components and Cu_2O/WO_3. After 24 h of light irradiation, the yields of CO, O_2 and H_2 reach 5.73, 2.79 and 0.34 μmol/(g·h), respectively, and good stability was maintained after 4 cycles (Figure 4(k)−(m)). This confirmed the synergistic effect between the (001) facet and the heterojunction. This study further verified that the (001) facet of WO_3 can serve as an efficient site for CO_2 adsorption and activation, while the heterojunction constructed with Cu_2O can enhance charge separation. The synergistic effect of these two factors endows the catalyst with both high activity and practicality.

1.5 Degradation of organic pollutant

WO_3-based semiconductor photocatalysts can effectively degrade a wide variety of organic dyes, including Methyl Orange (MO), Methylene Blue (MB), Alizarin Red S (ARS) and Rhodamine B (RhB)[53−54]. The type and proportion of its exposed crystal facets are among the core factors determining its degradation performance, which has been verified by numerous experimental studies and theoretical calculations[55]. In 2017, Wang et al.[56] synthesized WO_3 nanorods predominantly exposing (200) facet and WO_3 nanosheets with exposed (002) facet using sodium sulfate and ammonium sulfate as capping agents and under different hydrothermal conditions. They evaluated the photocatalytic activity of these materials using RhB as the target reactant, with the apparent rate constant (K_{app}) as the evaluation index. As shown in Figure 5(a), the K_{app} value of WO_3 nanosheets (W3) reaches 0.0115 min^{-1}, while that of WO_3 nanorods (W2) is only 0.0034 min^{-1}. Further analysis indicated that the (002) facet exhibited the best visible-light photocatalytic performance due to its highest surface energy, which was confirmed by DFT calculations.

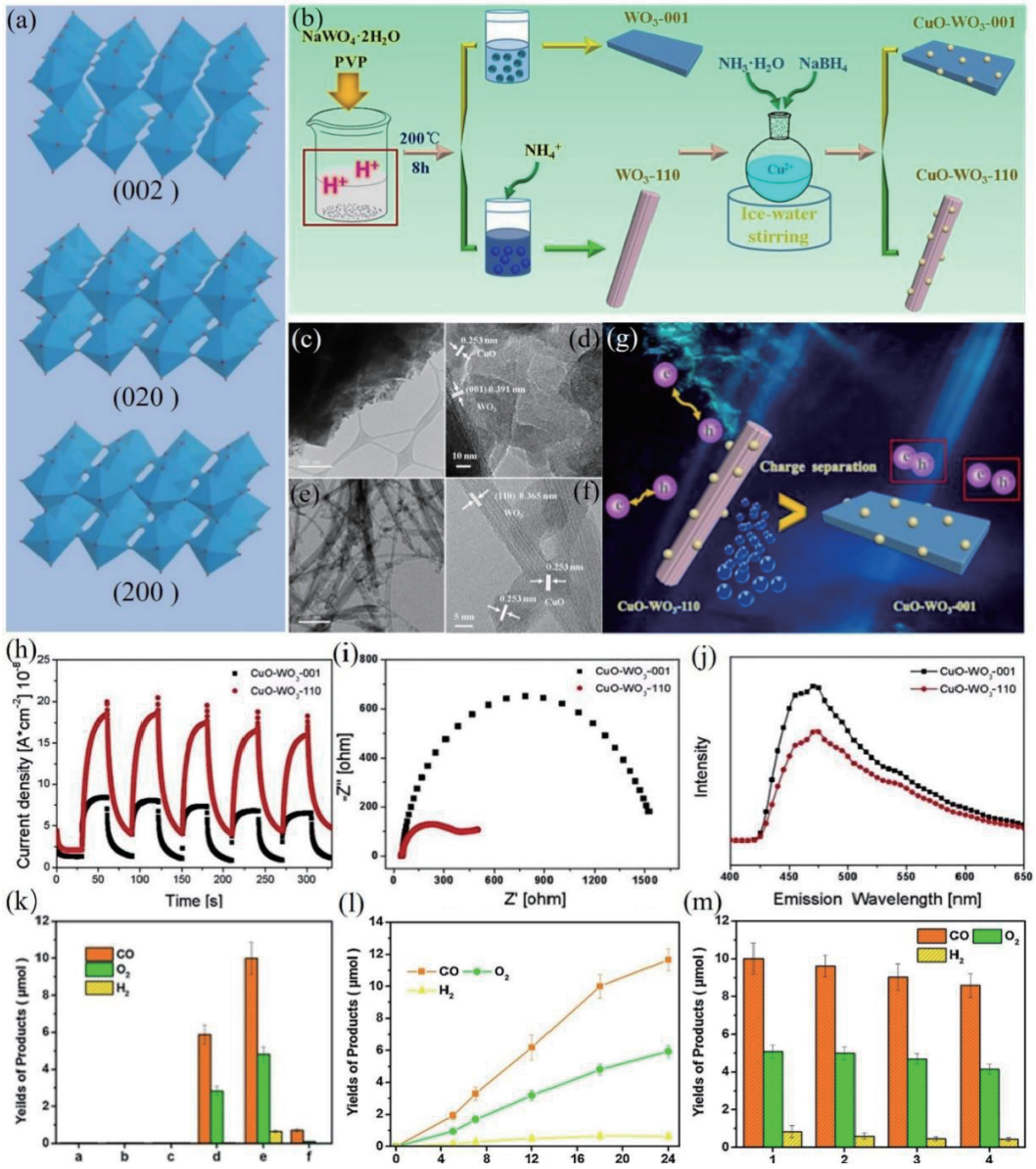


Fig. 4 (a) Crystalline model of the nanosheet[50]; (b) Schematic illustration of the preparation procedures of samples; (c), (d) TEM and HRTEM images of CuO-WO_3-001 nanosheets and (e), (f) CuO-WO_3-110 nanowires; (g) Schematic illustration of the charge separation; (h) Photocurrent response, (i) EIS and (j) PL spectra of both samples[51]; (k) Photocatalytic performance of CO_2 reduction over samples (Cu_2O a; WO_3 b; WO_3-001 c; Cu_2O/WO_3 d; Cu_2O/WO_3-001 e; Cu_2O/WO_3-001-m f); (l) Total yields of the products; (m) Recyclability test of Cu_2O/WO_3-001 catalyst[52]
(with permission from RSC Publications, Elsevier)

As shown in Figure 5(c), the surface energy of the WO_3(001) facet (equivalent plane of (002)) is 1.74 J/m^2, which is higher than that of the (100) and (010) facets (1.69 J/m^2). Moreover, the electron transfer efficiency on the electrode surface was characterized by EIS. Generally, the smaller the semicircle arc diameter of the EIS spectrum, the lower the electron transfer resistance, corresponding to higher separation and transport efficiency of photoexcited e^--h^+ pairs[57]. As shown in Figure 5(b), the arc radius on the EIS Nyquist plot of the W3 sample is the smallest, which proved that the (001) facet is more conducive to the separation of charge carriers. This property, together with the high surface energy, collectively endowed it with excellent photocatalytic performance.

Based on this, Zhang et al.[58] synthesized WO_3 nanocrystals with different exposure ratios of the (001) facet. They found that when the exposure ratio of the (001) facet was the highest, the K_{app} of RhB degradation by the material reached 0.526 h^{-1}, which was more than 5 times that of commercial WO_3 (0.060 h^{-1}). The research team attributed this performance advantage to the fact that the high-energy facet could generate reactive oxygen species (ROS) more efficiently and further reduce the recombination rate of photogenerated e^--h^+ pairs. This finally confirmed that the exposure ratio of the (001) facet in orthorhombic WO_3 nanocrystals was positively correlated

with their photodegradation efficiency. Lee et al.[33] prepared a WO_{AT}@PCN hybrid photocatalyst by combining porous g-C_3N_4 nanosheets (PCN) and WO_3 nanorods with exposed (001) facets WO_{AT} (WO_{AT} was synthesized using ammonium tungstate as the precursor), which demonstrated significantly enhanced performance for the degradation of oxytetracycline (OT) and naproxen (NP) pollutants under visible light compared with PCN, WO_{AT}, and WO_{ST} (WO_{ST} was synthesized using sodium tungstate as the precursor) with different exposed facets (Figure 5(d)−(g)). Furthermore, the hybrid catalyst exhibited excellent stability and reusability across multiple test runs. They attributed the remarkable photodegradation performance of this hybrid catalyst to three aspects: first, the (001) facets of WO_{AT}, inherently possess a high specific surface area and excellent charge separation properties; second, the hybrid system enables enhanced visible light absorption; and third, the S-scheme charge transfer pathway formed at the interface can effectively promote the separation of photoexcited charges and enhance the redox capabilities of the separated photoexcited electrons and holes. Wang et al.[59] prepared flower-shaped WO_3 architectures weaved up of ultrathin nanobelts with oriented (001) facets. Compared with the hydrothermal counterpart assembled by thick, individual WO_3 nanobelts, this (001) faceted flower-shaped WO_3 exhibited improved photocatalytic activity for the degradation of MO, with the reaction K_{app} enhanced by 2.1 fold. The separation and migration of photogenerated e^--h^+ pairs were characterized by PL spectroscopy. Generally, a lower PL intensity indicates a lower carrier recombination rate and thus a higher photocatalytic activity[60]. The sample exhibited the weakest PL intensity, demonstrating more efficient separation and transfer of photogenerated carriers. Combined with the photocurrent response tests, it showed a higher photocurrent density under simulated sunlight and maintained approximately 1.5 times the photocurrent density of the WO_3 thick, individual WO_3 nanorods after cycling. Additionally, it had a smaller arc radius in the EIS Nyquist plot. These results collectively confirmed that the highly active (001) facets in WO_3 can facilitate interfacial charge transfer.

Ding et al.[61] introduced a synergistic effect by constructing a composite system, and also found the key role of the facet effect. They prepared Ag/WO_3 composite catalysts *via in situ* photoreduction, where silver nanoparticles (Ag NPs) were selectively deposited on the surface of hexagonal WO_3 nanorods with different exposed facets. The degradation of RhB, MO and other organic pollutants was carried out under visible-light irradiation. The results showed that both the intrinsic charge separation property of the (001) facet on WO_3 nanorods and the surface plasmon resonance (SPR) effect of Ag NPs contributed to enhancing visible-light absorption and reducing the recombination of photogenerated electron-hole pairs.

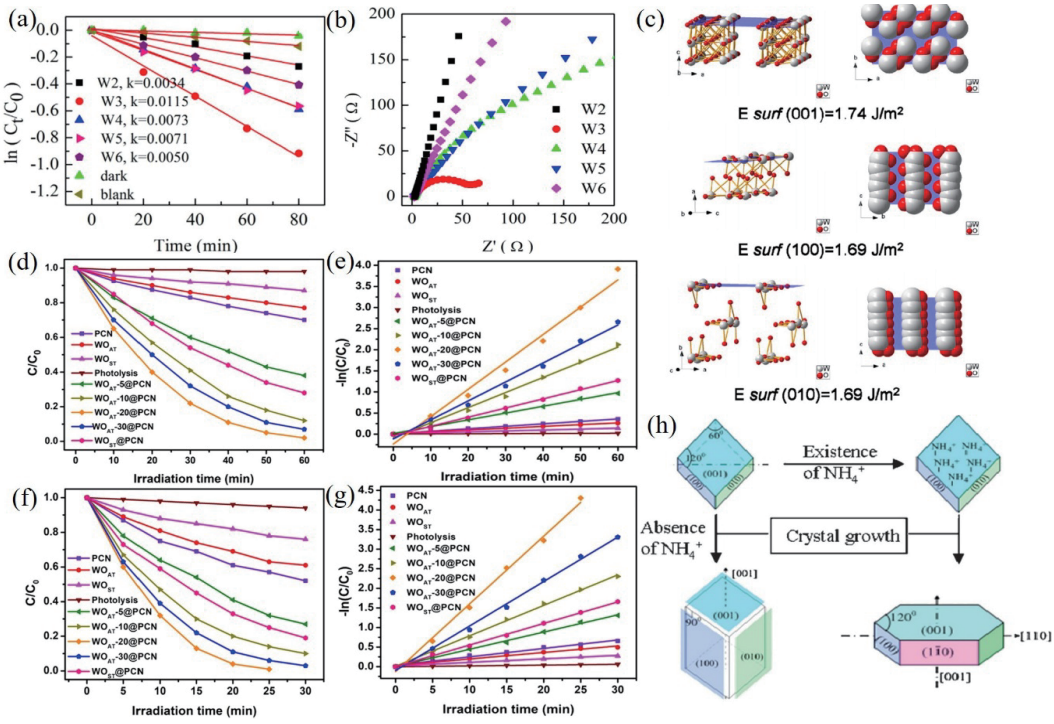


Fig. 5 (a) The first-order kinetics of RhB photocatalytic degradation over WO_3 photocatalysts and (b) their EIS[56]; (c) Schematic drawing of the crystal structure and 2D atom arrangement on the (001), (100) and (010) facets[58]; (d) and (f) Photocatalytic degradation performance comparison of the synthesized samples in terms of the removal of OT and NP; (e) and (g) The corresponding kinetics plots for OT and NP degradation[33]; (h) Illustration of the growth orientation of the hexagonal single crystal WO_3 nanorods[62] (with permission from Elsevier, RSC Publications)

Finally, the comparison indicated that the Ag/WO_3-001 composite catalyst with the (001) facet as the dominant exposed facet exhibited significantly better photocatalytic degradation activity than the Ag/WO_3-001 composite catalyst with the (100) and (010) facets as the main exposed facets.

Zhu et al.[62] focused on the regulation of the crystal orientation of hexagonal WO_3 nanorods, and prepared hexagonal WO_3 nanorods with two crystal orientations: [110] and [001] (Figure 5(h)). Their study reveals that hexagonal WO_3 nanorods grown along specific crystal orientations exhibited significant differences in exposed facets. Among them, the nanorods exposing the (001) facet had much higher adsorption capacities for RhB and MB than those exposing the (100) or (110) facet, which once again highlighted the structural advantage of the (001) facet in interacting with organic dye molecules.

In summary, the photocatalytic performance of WO_3 is directly influenced by its exposed facets, among which the (001) facet exhibits the most prominent superiority in the degradation of organic dyes, primarily attributable to its exceptionally high efficiency in separating photogenerated charge carriers. However, the underlying mechanism responsible for this highly efficient charge separation on the (001) facet has not been fully elucidated. Based on this, we speculate that since the (001) facet serves as the starting point for numerous lattice channels in WO_3, these intrinsic channels may induce differential transport behaviors for electrons and holes, thereby enabling effective spatial separation and consequently enhancing the photocatalytic activity.

2 Facet effect of WO_3 in electrocatalytic reactions

In the field of electrocatalysis, the (001) crystal facet of WO_3 demonstrates unique advantages. For example, to address the sluggish kinetics of conventional electrocatalytic nitrogen reduction reaction (NRR), Hou's team[63] developed a dual-driven nitrate electrocatalytic reduction (NO_3RR) system based on a Cu_1/WO_3 catalyst for sustainable NH_3 synthesis. They innovatively utilized nitrate pollutants (NO_3^-) as the nitrogen source for NH_3 production. The Cu_1/WO_3 catalyst was prepared *via* a simple wet-chemical method, where Cu single atoms were anchored onto the surface of WO_3 nanosheets predominantly exposing the (001) facet with rich in oxygen vacancies (Ov) (Figure 6(a), (c)). Characterization results revealed that the oxygen vacancies in WO_3 (WO_3-Ov) effectively stabilized the Cu atoms, forming a stable Cu-O-W coordination structure, which preserved the nanosheet morphology and enabled uniform distribution of Cu species (Figure 6(b)).

The core innovation of this system lay in its dual-driven mechanism design (Figure 6(d)): On one hand, WO_3 serves as a proton-driving center, with its (001) facet exhibiting excellent water dissociation capability (with an energy barrier of only 0.51 eV, much lower than 1.45 eV for Cu(111)), thereby continuously supplying protons for the reaction (Figure 6(e)). On the other hand, the electron-deficient Cu_1 sites (*d*-band center of −1.08 eV, higher than that of metallic Cu at −2.13 eV) act as nitrate activation centers, significantly enhancing the adsorption and activation of NO_3^- and its intermediates (Figure 6(f)).

Performance tests showed that Cu_1/WO_3 achieved an NH_3 production rate of 91 mmol/(g·h) at −0.60 V, with an NH_3 selectivity of 99.2% and a Faradaic efficiency of 93.7%, while generating only minimal nitrite by-products. Its overall performance surpassed that of most reported catalysts. Moreover, the catalyst maintained excellent stability after 2880 min of continuous operation and exhibits good tolerance to common impurity ions and organic compounds in water.

Meanwhile, Li et al.[64] synthesized ultrathin tungsten trioxide (WO_3) nanosheets for efficient electrocatalytic conversion of methane to ethanol. HRTEM images (Figure 6 (g)−(j)) showed lattice spacings of 0.366 and 0.372 nm, corresponding to the (200) and (020) planes of monoclinic WO_3, respectively. While the authors proposed the (010) facet as the predominantly exposed surface, further analysis suggested the (001) facet as the more likely active surface. A series of characterizations confirmed that this facet possesses the highest oxygen vacancy concentration. The WO_3 nanosheets achieved an exceptionally high ethanol production rate of 125.1 mmol/(g·h) with 99.4% selectivity at a low potential of 1.2 V *vs.* RHE over 8 h.

To elucidate the role of oxygen vacancies, the authors performed DFT calculations on pristine WO_3 (denoted as WO_3) and oxygen vacancy-rich WO_3 (denoted as Ov-WO_3), proposing possible reaction pathways for methane conversion on these surfaces. As shown in Figure 6(k), the $CH_4^* \rightarrow CH_3^*$ reaction is the key step in CH_4 oxidation. The presence of Ov lowers the energy barrier for this step by 0.92 eV, indicating that Ov-WO_3 facilitated CH_4 activation and initiation of the methane oxidative coupling (MEO) reaction more easily than WO_3. In the second step ($CH_3^* \rightarrow CH_2$), the carbon in CH_3^* could bind with two low-coordination W atoms around the Ov on the Ov-WO_3 surface, significantly reducing the dehydrogenation energy compared to WO_3 (−0.4 eV for Ov-WO_3 *vs.* 1.49 eV for WO_3). For Ov-WO_3, the rate-determining step was $CH_2^* \rightarrow CH_2OH$, with the largest energy change of 1.22 eV; whereas for WO_3, it was $CH_4 \rightarrow CH_3^*$, with an energy change of 1.5 eV, indicating a lower overall energy barrier for CH_4 oxidation on Ov-WO_3. The $CH_2OH^* + CH_3^* \rightarrow CH_3CH_2OH^*$ step was exothermic (with exothermicities of −1.4 eV for Ov-WO_3 and −2.34 eV for WO_3), favoring C–C bond coupling. In summary, oxygen vacancies on (001) facet served as key active sites, effectively promoted C–H bond activation and C–C coupling during methane conversion, thereby significantly enhanced electrocatalytic activity and ethanol selectivity. This study provided a constructive strategy for designing highly active and selective electrocatalysts for efficient methane conversion.

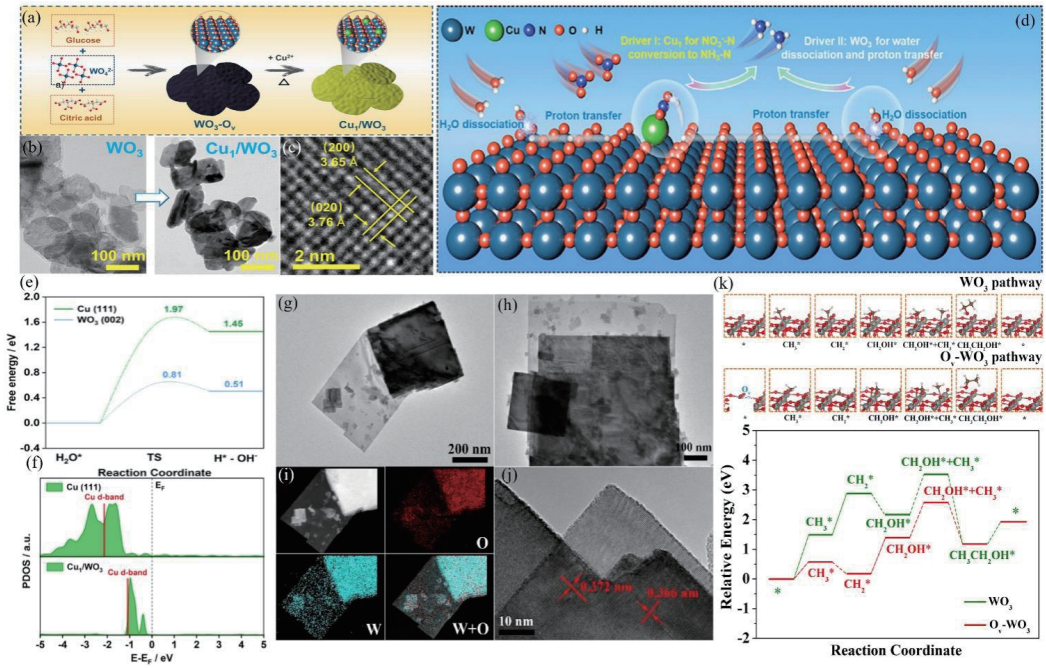


Fig. 6 (a) Schematic illustration of synthesis procedure for Cu_1/WO_3 catalyst; (b) TEM images of WO_3 and Cu_1/WO_3; (c) HRTEM image of Cu_1/WO_3; (d) Schematic illustration of the dual-driven NO_3RR mechanism; (e) Free energy profiles for water dissociation on Cu(111) and WO_3(002) at pH value 13.2, respectively; (f) Projected density of states (PDOS) for the Cu of Cu(111) and Cu_1/WO_3(002), respectively[63]; (g)–(j) Morphological and structural characterizations of S200/30 (Reaction time: 200 ℃, 30 h); (k) Reaction path and reaction energy profiles for CH_4 electrocatalytic oxidation to ethanol on the surfaces of WO_3 and Ov-WO_3 respectively[64] (with permission from John Wiley and Sons, Elsevier)

3 Facet effect of WO_3 in photoelectrocatalytic reactions

3.1 Water splitting

Photoelectrochemical (PEC) catalysis, which integrates the dual advantages of photocatalysis and electrocatalysis, has become as a pivotal technology for driving various chemical reactions[65–67]. Among them, PEC water splitting based on semiconductor photoelectrodes not only serves as an ideal and eco-friendly approach for H_2 production using renewable solar energy but also provides a critical pathway for the large-scale production of sustainable hydrogen fuel[68]. Over the past five decades, improving the solar-to-hydrogen (STH) conversion efficiency has remained a core objective in this field[69–71]. Against this backdrop, WO_3 is regarded as a highly promising visible-light-responsive photoanode material for PEC water splitting, owing to its environmental benignity, low cost, moderate hole diffusion length of 150 nm (which ensures efficient charge separation) and electron mobility of 12 $cm^2/(V·s)$ (which supports effective charge transport)[72–73]. However, its E_g (2.6–2.8 eV) results in a narrow light response range and low solar light harvesting efficiency. To overcome this limitation, researchers often optimize its performance through doping, heterojunction construction, or facet modification.

Wang et al.[74] successfully synthesized WO_3 nanosheets with exposed (200) and (002) facets, respectively, *via* a two-step hydrothermal method by precisely regulating the reaction time and procedures. As shown in Figure 7(a), among these samples, the WO_3 photoanode with exposed (002) facet (1-step-8 h, one-step hydrothermal method with a reaction time of 8 h) achieves a photocurrent density of 3.1 mA/cm^2 at 1.23 V *vs.* reversible hydrogen electrode (RHE), which is significantly higher than that of the sample with exposed (200) facet (2.1 mA/cm^2, 1-step-16 h, one-step hydrothermal method with a reaction time of 16 h). Meanwhile, the researchers investigated their photoresponsive properties and measured their chopped transient photocurrent density *vs.* time curves. In Figure 7 (b), the performance of the (200)-faceted sample degrades sharply after 400 seconds of intermittent light irradiation, whereas the (002)-faceted sample exhibits superior stability. They also evaluated their incident-photon-to-current conversion efficiencies (IPCE) across different wavelength ranges, as shown in Figure 7(c), the IPCE value of the 1-step-16 h photoanode is much lower than that of the 1-step-8 h photoanode, indicating that the exposed (002) facet of the 1-step-8 h photoanode is more conducive to the separation of photoexcited electron-hole pairs.

Liu et al.[75] prepared WO_3 with e^--rich edge (020)/(200) facet and h^+-rich (002) facet. They then rationally modified the WO_3 surface with Ag nanoparticles and ZnFe layered double hydroxides (ZnFe-LDHs) to construct an Ag/WO_3/ZnFe-LDH composite photoanode (Figure 7(d)). After 4000 s of continuous illumination, the current density of this photoanode remains stable (Figure 7(e)). It achieves

a maximum photocurrent density of 1.18 mA/cm^2 at 1.23 V *vs.* RHE, which is 14.4 times higher than that of WO_3 without preferential facet orientation (Figure 7(f)). More importantly, it realized an average H_2 production rate of 38.18 μmol/h in natural seawater splitting and exhibited excellent photoelectrochemical stability. As shown in Figure 7(g), the faradaic efficiency of hydrogen evolution in this system is nearly 100%. This successfully addresses the long-standing issues of poor corrosion resistance and low efficiency of traditional photoelectrodes in seawater.

Liu et al.[76] investigated the underlying mechanism of crystal facet-dependent properties mentioned above. They synthesized four types of WO_3 thin films with different facet orientations (200-WO_3, plate-like WO_3, 002-WO_3 and thin-flake WO_3) and deposited $BiVO_4$ on their surfaces to construct heterojunctions for PEC water splitting. The results revealed that the Fermi energy of WO_3 exhibits a distinct facet dependence: 200-WO_3 has the highest Fermi energy (5.47 eV), 002-WO_3 the lowest (5.18 eV), while plate-like and thin-flake WO_3 shows intermediate values between these two extremes. This difference directly alters the flat-band potential of the WO_3/$BiVO_4$ heterojunction—a key parameter influencing the difficulty of initiating PEC reactions. Specifically, the heterojunction constructed with (002)-dominant WO_3 exhibits a more negative flat-band potential due to the lower Fermi energy of (002)-WO_3, leading to a reduced onset potential of 0.868 V *vs.* RHE in PEC tests. This not only significantly lowers the reaction energy consumption but also improves the energy conversion efficiency of the device, thus clarifying the intrinsic mechanism of facet orientation in regulating heterojunction performance from the perspective of electronic structure.

These studies provide clear insights for the structural design and performance optimization of semiconductor optoelectronic devices and hold great significance for advancing the development of efficient, stable, and practical PEC water splitting technologies.

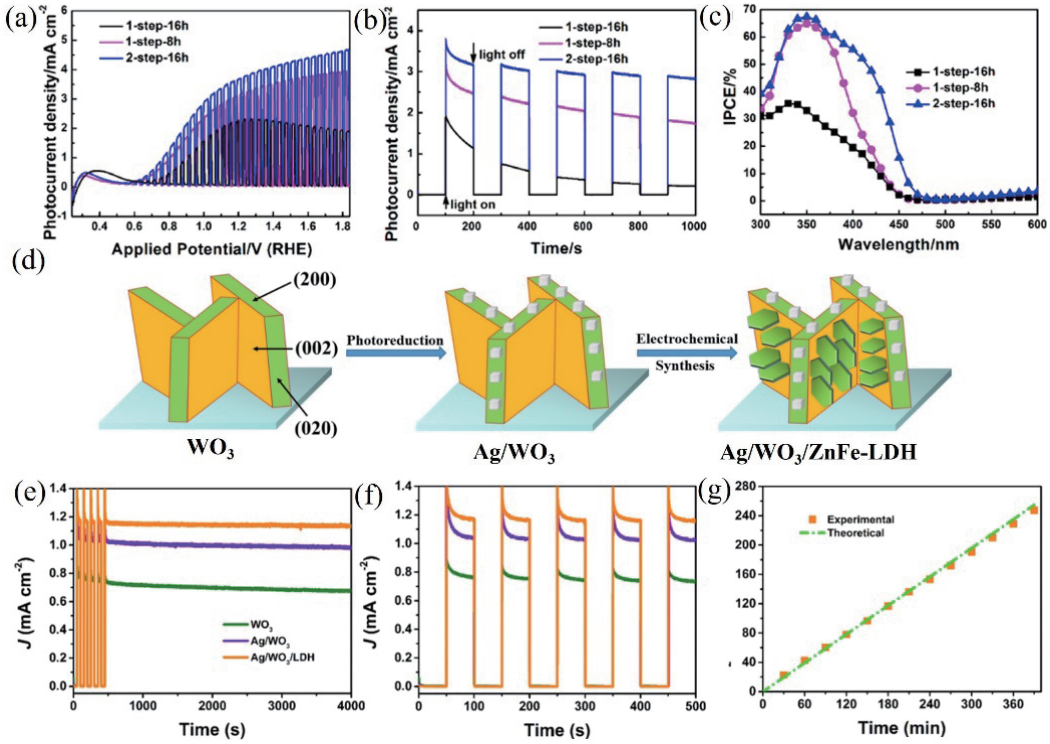


Fig. 7 (a) Photocurrent density *vs.* applied potential curves and (b) *vs.* time measured at 1.23 V *vs.* RHE, (c) IPCE spectra of the 1-step-16 h (black curves), 1-step-8 h (magenta curves) and 2-step-16 h (blue curves) photoanodes; (d) Schematic illustration for the fabrication of Ag/WO_3/ZnFe-LDH NSAs; (e) Photocurrent–potential curves of different samples under illumination; (f) Amperometric *I*–*t* curves; (g) Total H_2 production detected by a gas chromatograph[74−75]
(with permission from Elsevier)

3.2 Conversion of methane into ethylene glycol

The utilization of methane as a feedstock for the production of value-added chemicals (such as C_2H_6, CH_3OH and HCOOH) represents an important direction in energy catalysis. However, the high stability and inertness of the C–H bond in methane molecules pose significant challenges for its PEC conversion, especially in achieving high selectivity toward C_{2+} products[77−79]. Xiong's team[80] successfully achieved highly efficient PEC methane conversion under mild conditions without external oxidants through facet tuning strategies. Their study first applied DFT calculations to systematically compare the adsorption behaviors of hydroxyl radicals (·OH)—key reactive species—on different facets ((010), (100) and (001)) of monoclinic WO_3. Figure 8(a) shows the lowest-energy

adsorption configurations of ·OH on these three facets. The calculated adsorption energies are −1.742, −1.826 and −1.935 eV, respectively. Although ·OH exhibits strong adsorption on all three facets, both its configuration and reactivity demonstrate distinct facet-dependent behaviors: For (100) facet, two adsorbed ·OH are spatially close (1.872 Å) forming hydrogen bond; for (001) facet, ·OH is further converted into H_2O and surface-bound oxygen species; whereas for (010) facet, the vast distance (3.342 Å) effectively suppresses hydrogen bonding and side reactions, thereby preserving the high reactivity of ·OH and facilitating C–H bond activation in methane.

To verify the facet-dependent effects, they designed WO_3 photoanodes with graded (010) facet exposure ratios (nanobars, NB; nanoplates, NP; and nanoflakes, NF), as shown in Figure 8(b), (c). EPR (Electron paramagnetic resonance) measurements using 5,5-dimethyl-1-pyrroline N-oxide (DMPO) as a spin-trapping agent were performed to detect ·OH generated on the prepared WO_3 photoanodes. As shown in Figure 8(d), the DMPO-·OH adduct signal intensity follows the order WO_3 NB > WO_3 NP > WO_3 NF, indicating that the ·OH production rate correlates positively with the ratio of (010) facets. Among the tested photoanodes, the WO_3 nanobars with the highest proportion of (010) facets exhibited the best performance in PEC methane conversion. At an applied potential of 1.3 V *vs.* RHE, the ethylene glycol production rate reaches 0.47 mmol/(cm^2·h), with a selectivity of 66% and a Faradaic efficiency of 23.9%—2.5 times higher than that of nanoflakes. At applied potentials of 1.1 and 1.3 V *vs.* RHE, STF efficiencies of 0.10% and 0.12% are achieved, respectively, with a carbon balance >90% (Figure 8(e), (f)). Furthermore, the system demonstrated high stability over 12 h of PEC methane oxidation. This study highlights the critical role of facet regulation in enhancing radical reactivity and product selectivity, providing new insights for the design of efficient photoanodes for methane conversion.

4 Facet effect of WO_3 in thermocatalytic reactions

In recent years, the application of WO_3 as an acid catalyst has attracted significant attention, and its catalytic activity is closely related to the distribution of surface acid sites[81−82]. It has been widely employed in various reactions such as olefin metathesis, epoxidation and isomerization[83−85], yet investigations into the facet effect have not been conducted in these reactions to date, which constitutes a promising research direction for the future.

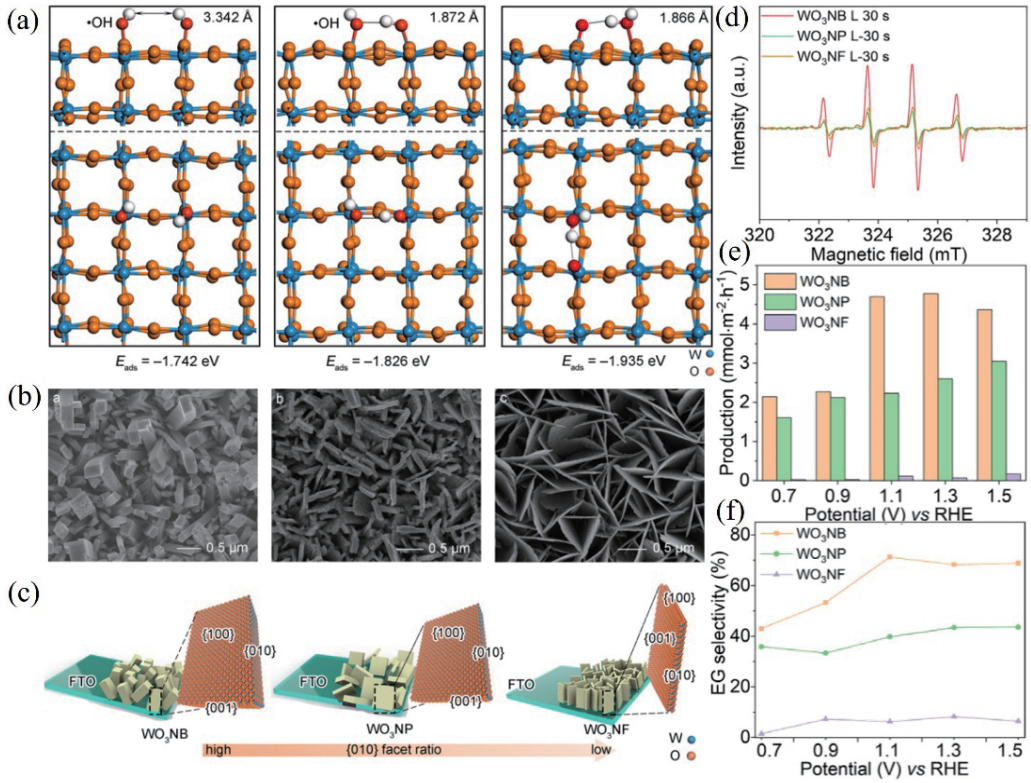


Fig. 8 (a) The atomic structures of ·OH adsorption on twinning W atoms of (010), (100) and (001) facets; (b) SEM images of WO_3 NB, WO_3 NP and WO_3 NF; (c) Schematic illustration for monoclinic WO_3 nanostructures with different (010) facet ratios on substrates; (d) EPR detection of ·OH using DMPO as a spin-trapping agent of WO_3 NB, WO_3 NP and WO_3 NF; (e) Production rate and (f) carbon selectivity of EG produced in PEC CH_4 conversion on WO_3 photoanodes with different (010) facet ratios at a range of potentials under 100 mW/cm^2 illumination[80]
(with permission from John Wiley and Sons)

Relevant research on the facet effect that has been reported so far is as follows. Gao et al.[86] investigated the catalytic conversion of furfuryl alcohol (FA) to ethyl levulinate (EL) over WO_3 with different exposed crystal facets (nanosheets with the (001) facet, nanobelts with the (100) facet, and nanoparticles with the (110) facet, see Figure 9(a)−(c) in an ethanol system). WO_3 with the (110) facet achieves an EL production rate of 4.7 mmol/(g·h) at 170 °C, while WO_3 with the (100) and (001) facets mainly converts FA into polymers.

The study pointed out that this difference stems from the varying characteristics of acid sites on different crystal facets. Specifically, the (110) facet not only has a higher total number of atoms and a higher proportion of W atoms but also is rich in high-valence W^{6+} species and W=O bonds with high binding energy, which significantly enhances its surface acidity. This facet possesses both strong Brønsted acid sites (BAS) and Lewis acid sites (LAS): the former can provide protons, while the latter promotes the adsorption of reactant molecules. The synergistic effect of these two types of acid sites efficiently facilitates the conversion of FA to EL (Figure 9(d)).

In contrast, the (100) facet has a high proportion of W atoms but a small total number of atoms. Although it is favorable for the formation of LAS, the acid strength is weak. Due to the dominance of strong LAS and the weakness of BAS, it tends to cause FA to form polymers. The (001) facet has a large total number of atoms but a high oxygen proportion and low binding energy of W^{6+}, which is not only unfavorable for the exposure of W atoms but also inhibits the formation of hydroxyl groups, resulting in only weak LAS and BAS.

In addition, the (110) facet catalyst exhibits better sustainable catalytic performance than the (100) facet catalyst. All the above conclusions were verified by characterization techniques such as FT-IR and NH_3-TPD (Figure 9(e)−(h)).

The facet effect of WO_3 was not only observed in heterogeneous catalytic reactions but also applicable in the field of gas sensing involving chemical conversion. In the field of gas sensing, WO_3-based materials have attracted significant research interest due to their high sensitivity and selectivity[87−88]. Yin et al.[89] synthesized thickness-controlled rectangular WO_3 nanosheets predominantly exposing (020) and (200) facets *via* a low-temperature acid-assisted (hydrochloric acid) hydrothermal method followed by thermal treatment. The resulting samples a1, a2 and a3 had average thicknesses of approximately 110, 70 and 10 nm, respectively, with the (020) facet exposure ratio following the order a3 > a1 > a2. The sensors prepared using samples a1, a2 and a3 are labeled as sensor 1, sensor 2 and sensor 3, respectively. It was found that the gas-sensing response to acetone significantly increased with higher exposure of the (020) facet, demonstrating distinct facet-dependent behavior.

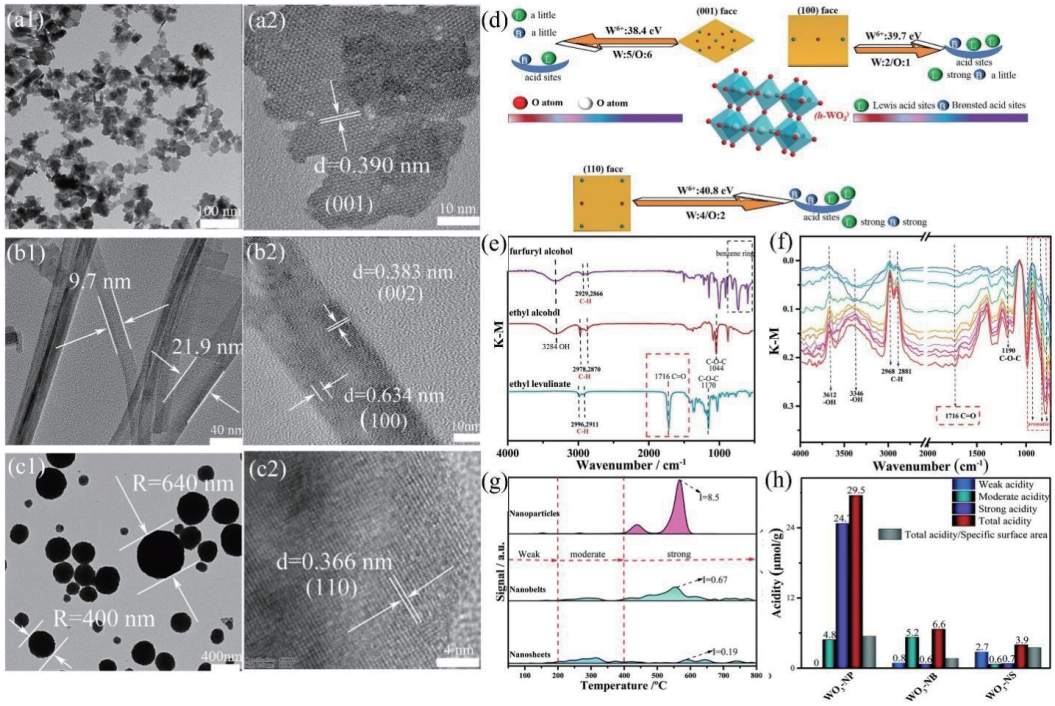


Fig. 9 TEM and HRTEM images of (a1, a2) WO_3 nanosheets, (b1, b2) WO_3 nanobelts, (c1, c2) WO_3 nanoparticles; (d) Relationship between the WO_3 catalyst structure and acid site distribution; (e) FT-IR spectra of furfuryl alcohol, ethyl alcohol, and ethyl levulinate; (f) FT-IR changes in the conversion of furfuryl alcohol to ethyl levulinate at 150 ℃ in N_2 (from top to bottom, the curves correspond to the following reaction times: 5, 10, 15, 20, 25, 30, 32, 35, 38, 40 min); (g) NH_3-TPD spectra of the WO_3 catalysts with different morphologies; (h) Distribution of acidic sites over the WO_3 catalysts with different morphologies obtained by NH_3-TPD[85] (with permission from RSC Publications)

As shown in Figure 10(a)−(c), when tests at their respective optimal operating temperatures toward 1.0×10^{-4} of various gases, sensor 3 exhibits superior acetone sensing performance: a high response value of 49.1. As shown in Figure 10(d), at the same gas concentration, sensor 3 exhibits the highest response intensity. Meanwhile, it has a low detection limit of 5.0×10^{-7} (Figure 10(e)) and rapid response/recovery times of 7 and 19 s, respectively. The sensing mechanism was further discussed, suggesting that the abundant dangling bonds and localized electric polarization on specific exposed facets may be key factors contributing to the high sensitivity and selectivity toward acetone.

On the other hand, addressing the need for detecting toxic, volatile, and flammable triethylamine (TEA) in industrial settings, Wang et al.[90] prepared a series of WO_3 samples (denoted as C1-400, C2-400, C4-400 and C6-400) using alcohols with different carbon chain lengths (methanol, ethanol, *n*-butanol, cyclohexanol) as solvents, combined with solvothermal pretreatment at 180 °C and subsequent calcination at 400 °C in air. XRD quantitative analysis of normalized intensity ratios of characteristic facets revealed that the (002) facet intensity ratio of C2-400 was significantly lower than those of other samples. Meanwhile, UPS (Ultraviolet Photo-electron Spectroscopy) characterization combined with W_f (work function) calculations indicated that C2-400 possessed a notably higher W_f (Figure 10(g)−(i)). This phenomenon was attributed to surface electronic restructuring induced by the lowest proportion of the (002) facet. A higher W_f requires more energy to excite electrons for participation in gas-sensing reactions, which correlates well with the optimal operating temperature of C2-400 at 325 °C—significantly higher than those of C1-400 (275 °C) and C4-400 (250 °C). As shown in Figure 10(f), at this temperature, C2-400 exhibits a high response value, excellent selectivity, fast response/recovery (3 s/5 s) to 1.0×10^{-6} TEA, and a detection limit as low as 2.0×10^{-7}, well below the ACGIH threshold of 1.0×10^{-6}. These results fully demonstrated the critical role of facet structure in regulating electronic properties and gas-sensing behavior.

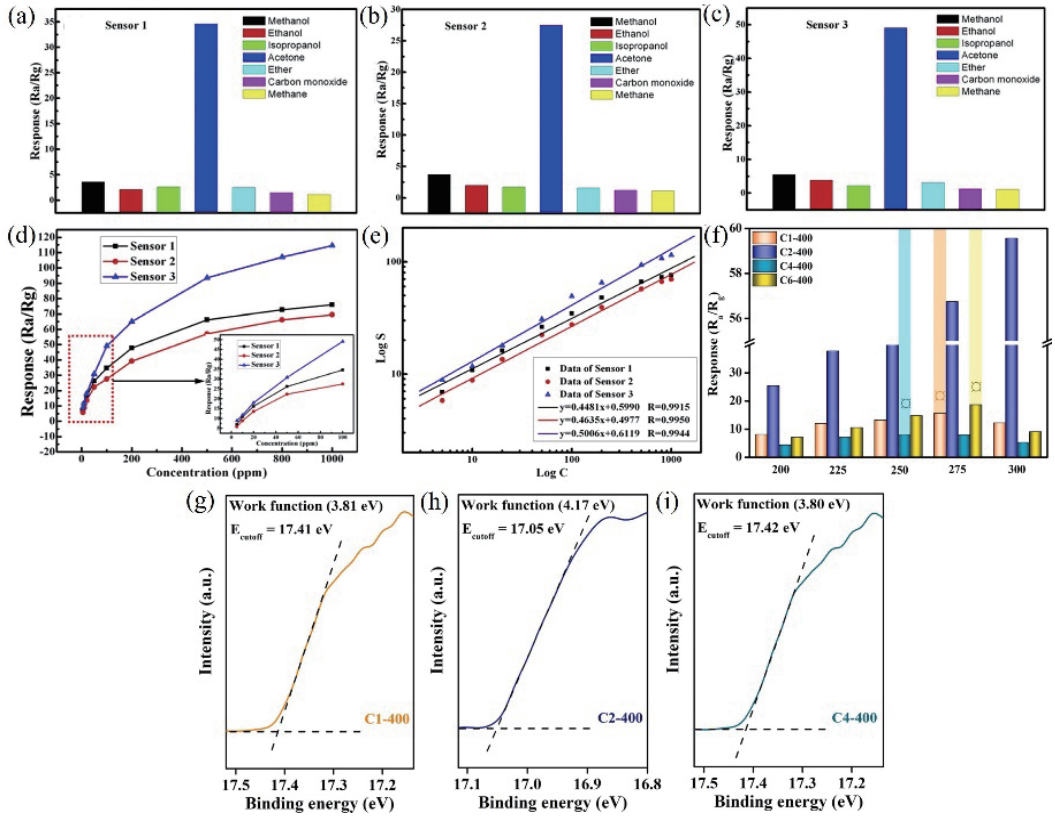


Fig. 10 (a)−(c) Responses of the sensors to 1.0×10^{-4} various gases; (d) Acetone response plots of the sensors from 5.0×10^{-6}–1.0×10^{-3} (The inset is an enlarged image of the dashed box part); (e) The corresponding logarithm fit curves[89] of sensor 1, sensor 2 and sensor 3 with (020) facet increasing; (f) Responses of the sensors based on C1-400, C2-400 (more (002) facet), C4-400 and C6-400 upon exposure to 1.0×10^{-4} TEA in different operating temperatures; (g)−(i) UPS spectra of the C1-400, C2-400 and C4-400 samples[90] (with permission from Elsevier)

5 Summary and outlook

This review systematically elucidates the facet-dependent effects of WO_3 nanocrystals in heterogeneous catalytic systems, including photocatalysis, electrocatalysis, photoelectrocatalysis, and thermal catalysis. In the field of photocatalysis, the interfacial charge separation

characteristics and electronic structure differences of WO_3 determine its activity in water oxidation, benzyl alcohol oxidation, N_2 fixation, and CO_2 reduction. DFT calculations revealed that the (110) facet exhibits outstanding performance in benzyl alcohol oxidation due to the synergistic advantages of its lower effective hole mass, higher hole mobility, and longer hole diffusion length. In organic pollutant degradation reactions, the (002) facet demonstrates excellent photogenerated charge carrier separation and transport properties, attributed to its highest surface energy and the minimal electron transfer resistance confirmed by EIS. In electrocatalytic oxygen evolution, the (001) facet shows remarkable performance owing to its high specific surface area and optimized adsorption energy. In photoelectrocatalysis methane conversion, DFT calculations uncover the differences in·OH adsorption behavior across various crystal facets, clarifying the regulating mechanism of facet structure on reaction pathways. In thermal catalysis, the (110) facet achieves superior catalytic efficiency through the synergistic effect of its unique Brønsted and Lewis acid sites. In gas sensing applications, the (020) facet shows high selectivity toward molecules such as triethylamine and acetone, owing to its excellent gas adsorption capacity and redox properties.

However, current research predominantly remains at the level of phenomenological description and fragmented attribution of performance differences among crystal facets. Although various characterization techniques have partially established "structure-property" correlations, studies have yet to deeply elucidate the unified physicochemical mechanisms underlying the facet effects or extract universal structure-activity relationships.

Despite significant progress, several challenges remain in the study of facet effects in WO_3: (1) The controllable synthesis of high-index facets remains challenging; (2) Theoretical understanding of the atomic arrangement, dangling bonds, and electronic structure of different facets is insufficient; (3) The coupling effects of size, facet synergy, and interfacial charge behavior are often overlooked; (4) Research on facet effects in thermal and electrocatalysis is still relatively limited. Future research should focus on developing precise facet control strategies, combining *in situ* characterization and theoretical calculations to reveal interfacial reaction mechanisms, expanding the application of facet effects to more catalytic systems, and promoting the design of practical catalysts.

Based on literature researches, we have summarized the current representative performance benchmarks across various catalytic fields, providing important reference data for the evaluation of catalytic materials. (1) In the field of photocatalysis, under visible light, the highest oxygen evolution rate for photocatalytic water oxidation can reach 631.33 mmol/(g·h), with an oxygen evolution quantum efficiency of 84% at a wavelength of 400 nm. For the oxidation of benzyl alcohol to benzaldehyde, the optimal catalyst achieves a benzaldehyde production rate of 23.068 mmol/(g·h) and a conversion rate as high as 99%. The highest reported NH_3 production rate for photocatalytic nitrogen fixation is 521.37 μmol/(g·h). For photocatalytic CO_2 reduction, the CO production rate can reach 1.7×10^6 μmol/(g·h). In the field of organic pollutant degradation, the K_{app} values for the degradation of MO and RhB can be as high as 0.05 min^{-1}. (2) In the field of electrocatalysis, nitrate-to-ammonia synthesis can achieve 100% ammonia selectivity and a Faradaic efficiency exceeding 98%, with an ammonia production rate of 1.18×10^4 mmol/(g·h). (3) In the field of photoelectrocatalysis water splitting, the highest reported photocurrent density reaches 4.8 mA/cm^2 (at 1.23 V *vs.* RHE) with excellent stability exceeding 120 h. (4) In thermocatalysis, the production rate of ethyl levulinate (EL) from thermocatalytic conversion of furfuryl alcohol reaches 9.61 mmol/(g·h). Moreover, in electrochemical sensing, the lowest detection limit for acetone is as low as 5.0×10^{-8}, and for triethylamine, it reaches 1.0×10^{-7}. Considering the above reference values, the catalytic performance of WO_3 exhibits clear field-specific disparities. In photoelectrocatalytic and electrocatalytic methane conversion systems, the current performance of WO_3 is at a high level, whereas in other catalytic fields, its performance is generally at a medium level. This review primarily emphasizes how the facet effects of WO_3 influence its catalytic behavior from a mechanistic perspective. Therefore, the selected case studies aim to demonstrate how different facet exposures significantly alter catalytic performance trends and selectivity. To further enhance the catalytic performance of WO_3 across various fields in the future, strategies such as doping and modification can be employed to optimize its electronic structure and surface active site properties, providing a reference direction for subsequent performance optimization research.

In summary, the study of facet effects in WO_3 is evolving from macroscopic performance regulation to atomic-level mechanistic understanding. Through multidisciplinary collaboration and advanced characterization techniques, breakthroughs in both fundamental theory and practical applications can be anticipated.

Declaration of Competing Interest

The authors declare no conflict of interest.

References

[1] ERTL G, FREUND H J. Catalysis and surface science[M]. New York: American Institute of Physics, 1999, 52(1): 32−38.

[2] SHAIKH I P. Organocatalysis: Key trends in green synthetic chemistry, challenges, scope towards heterogenization, and importance from research and industrial point of view[J]. J Catal, 2014, 2014(1): 402860.

[3] VAYENAS C G, TSOUSIS D G, MARTINO E H. Catalysis in Chemistry and Physics[M]. Berlin: Springer, 2024:

147−180.

[4] MA L, LIU J. Catalytic nucleic acids: Biochemistry, chemical biology, biosensors, and nanotechnology[J]. Iscience, 2020, 23(1): 100815.

[5] RODUNER E. Understanding catalysis[J]. Chem Soc Rev, 2014, 43(24): 8226−8239.

[6] AKHTAR M S, ALI S, ZAMAN W. Recent advancements in catalysts for petroleum refining[J]. Catalysts, 2024, 14(12): 841.

[7] ELLIS L D, RORRER N A, SULLIVAN K P, et al. Chemical and biological catalysis for plastics recycling and upcycling [J]. Nat Catal, 2021, 4(7): 539−556.

[8] XU J, YANG Y, LI Y. Recent development in converting coal to clean fuels in China[J]. Fuel, 2015, 152: 122−130.

[9] LIU Y, ZHANG W, CHEN W. Denitrification technology and the catalysts: A review and recent advances[J]. ChemCatChem, 2024, 16(15): e202301662.

[10] WACLAWEK S, PADIL V V T, CERNIK M. Major advances and challenges in heterogeneous catalysis for environmental applications: A Review[J]. Ecol Chem Eng S, 2018, 25(1): 9−34.

[11] VEDRINE J C. Metal oxides in heterogeneous oxidation catalysis: State of the art and challenges for a more sustainable world[J]. ChemSusChem, 2019, 12(3): 577−588.

[12] XIE X, SHEN W. Morphology control of cobalt oxidenanocrystals for promoting their catalytic performance [J]. Nanoscale, 2009, 1(1): 50−60.

[13] HU J, CHEN L, RICHARDS R. Properties, synthesis and applications of highly dispersed metal oxide catalysts[J]. Metal Oxide Catal, 2008: 613−663.

[14] PAL J, PAL T. Faceted metal and metal oxide nanoparticles: Design, fabrication and catalysis[J]. Nanoscale, 2015, 7(34): 14159−14190.

[15] LI Y, SHEN W. Morphology-dependent nanocatalysts: Rod-shaped oxides[J]. Chem Soc Rev, 2014, 43(5): 1543−1574.

[16] LIU G, YU J, LU G, et al. Crystal facet engineering of semiconductor photocatalysts: Motivations, advances and unique properties[J]. Chem Comm, 2011, 47(24): 6763−6783.

[17] LUO J, ZHANG S, SUN M, et al. A critical review on energy conversion and environmental remediation of photocatalysts with remodeling crystal lattice, surface, and interface[J]. ACS Nano, 2019, 13(9): 9811−9840.

[18] HUO Z, CHEN C, LIU X, et al. One-pot synthesis of monodisperse CeO_2 nanocrystals and superlattices[J]. Chem Commun, 2008, (32): 3741−3743.

[19] YAO Y, SANG D, ZOU L, et al. A review on the properties and applications of WO_3 nanostructure-based optical and electronic devices[J]. Nanomaterials, 2021, 11(8): 2136.

[20] LI X, FU L, KARIMI-MALEH H, et al. Innovations in WO_3 gas sensors: Nanostructure engineering, functionalization, and future perspectives[J]. Heliyon, 2024, 10(6): e27740.

[21] HARIHARAN V, GNANAVEL B, SATHIYAPRIYA R, et al. A review on tungsten oxide (WO_3) and their derivatives for sensor applications[J]. Int J Adv Sci Eng, 2019, 5(4): 1163−1168.

[22] WANG J, CHAI J, DANG W, et al. Molecular dynamics study on melting point of tungsten nanostructures[J]. Nucl Mater Energy, 2022, 33: 101260.

[23] DEB S K. Opportunities and challenges in science and technology of WO_3 for electrochromic and related applications[J]. Sol Energy Mater Sol Cells, 2008, 92(2): 245−258.

[24] WU Z, LI Y, YAN Q, et al. Gamma radiation shielding properties of WO_3/Bi_2O_3/waterborne polyurethane composites [J]. J Korean Phys Soc, 2022, 81(3): 199−205.

[25] DONG Y, CHANG S, ZHANG H, et al. Effects of WO_3 particle size in WO_3/epoxy resin radiation shielding material[J]. Chin Phys Lett, 2012, 29(10): 108102.

[26] SHAO J, FENG S, LIU M, et al. Promising coloration composite strategy to multicolor photochromism for on - demand information displays[J]. Adv Funct Mater, 2025, 35(27): 2425059.

[27] GUI Y, YANG L, TIAN K, et al. P-type Co_3O_4 nanoarrays decorated on the surface of n-type flower-like WO_3 nanosheets for high-performance gas sensing[J]. Sens Actuators B Chem, 2019, 288: 104−112.

[28] LIN R, WAN J, XIONG Y, et al. Quantitative study of charge carrier dynamics in well-defined WO_3 nanowires and nanosheets: Insight into the crystal facet effect in photocatalysis[J]. J Am Chem Soc, 2018, 140(29): 9078−9082.

[29] KIMURA Y, MIURA H, TSUKAMOTO K, et al. Interferometric in-situ observation during nucleation and growth of WO_3 nanocrystals in vapor phase[J]. J Cryst Growth, 2011, 316(1): 196−200.

[30] MOHAMMAD-HOSSEINPOUR M, YOURDKHANI A, POURSALEHI R. Fast-switching electrochromic response of $WO_3 \cdot 2H_2O$ of plate-like particles synthesized by liquid phase deposition[J]. J Alloys Compd, 2021, 879: 160418.

[31] PFEIFER J, CAO G, TEKULA-BUXBAUM P, et al. A reinvestigation of the preparation of tungsten oxide hydrate WO_3, $1/3H_2O$[J]. J Solid State Chem, 1995, 119(1): 90−97.

[32] ZHENG J, SONG G, HONG J, et al. Facile fabrication of WO_3 nanoplates thin films with dominant crystal facet of (002) for water splitting[J]. Cryst Growth Des, 2014, 14(11): 6057−6066.

[33] LEE D E, REDDY K P, MORU S, et al. Facet-induced charge transfer and photocatalytic performance of an S-scheme hybrid heterojunction composed of porous g-C_3N_4 nanosheets and WO_3 nanorods with exposed high-energy (001) facets[J]. Appl Surf Sci, 2023, 610: 155569.

[34] PELEYEJU M G, AROTIBA O A. Recent trend in visible-light photoelectrocatalytic systems for degradation of organic contaminants in water/wastewater[J]. Environ Sci: Water Res Technol, 2018, 4(10): 1389−1411.

[35] TAHIR M B, NABI G, RAFIQUE M, et al. Nanostructured-based WO_3 photocatalysts: Recent development, activity enhancement, perspectives and applications for wastewater

treatment[J]. Int J Environ Sci Technol, 2017, 14(11): 2519−2542.

[36] ZHANG P, WANG T, CHANG X, et al. Effective charge carrier utilization in photocatalytic conversions[J]. Acc Chem Res, 2016, 49(5): 911−921.

[37] LI Z, XU X, SHENG X, et al. Solar-powered sustainable water production: State-of-the-art technologies for sunlight–energy–water nexus[J]. ACS nano, 2021, 15(8): 12535−12566.

[38] GONG H, ZHANG Y, CAO Y, et al. Pt@Cu_2O/WO_3 composite photocatalyst for enhanced photocatalytic water oxidation performance[J]. Appl Catal B: Environ, 2018, 237: 309−317.

[39] WANG F, YANG Z, YANG Z, et al. Graphene triggered hole activation strategy for 2D/2D-Layered (001)/(100)WO_3 facet junction towards enhanced photocatalytic water oxidation kinetics[J]. Chem Eng J, 2022, 450: 138166.

[40] GILLET S, AGUEDO M, PETITJEAM L, et al. Lignin transformations for high value applications: Towards targeted modifications using green chemistry[J]. Green Chem, 2017, 19(18): 4200−4233.

[41] ASHRAF M, AYAZ M, KHAN M, et al. Recent trends in sustainable solar energy conversion technologies: Mechanisms, prospects, and challenges[J]. Energy Fuels, 2023, 37(9): 6283−6301.

[42] YUAN J, YI X, TANG Y, et al. Efficient photocatalytic nitrogen fixation: Enhanced polarization, activation, and cleavage by asymmetrical electron donation to N≡N Bond[J]. Adv Funct Mater, 2020, 30(4): 1906983.

[43] LI P, ZHOU Z, WANG Q, et al. Visible-light-driven nitrogen fixation catalyzed by Bi_5O_7Br nanostructures: Enhanced performance by oxygen vacancies[J]. J Am Chem Soc, 2020, 142(28): 12430−12439.

[44] ZHAO Y, ZHAO Y, SHI R, et al. Tuning oxygen vacancies in ultrathin TiO_2 nanosheets to boost photocatalytic nitrogen fixation up to 700 nm[J]. Adv Mater, 2019, 31(16): 1806482.

[45] HONKALA K, HELLMAN A, REMEDIAKIS I N, et al. Ammonia synthesis from first-principles calculations[J]. Science, 2005, 307(5709): 555−558.

[46] XIONG L, HU Y, YANG Y, et al. Electron pump strengthened facet engineering: Organic half-metallic $C(CN)_3$ enclosed (100) facet exposed WO_3 for efficient and selective photocatalytic nitrogen fixation[J]. Appl Catal B: Environ, 2022, 317: 121660.

[47] ROY S C, VARGHESE O K, PAULOSE M, et al. Toward solar fuels: Photocatalytic conversion of carbon dioxide to hydrocarbons[J]. ACS Nano, 2010, 4(3): 1259−1278.

[48] ZHOU Y, TIAN Z, ZHAO Z, et al. High-yield synthesis of ultrathin and uniform Bi_2WO_6 square nanoplates benefitting from photocatalytic reduction of CO_2 into renewable hydrocarbon fuel under visible light[J]. ACS Appl Mater Interfaces, 2011, 3(9): 3594−3601.

[49] YANG G, ZHU X, CHENG G, et al. Engineered tungsten oxide-based photocatalysts for CO_2 reduction: Categories and roles[J]. J Mater Chem A, 2021, 9(40): 22781−22809.

[50] XIE Y, LIU G, YIN L, et al. Crystal facet-dependent photocatalytic oxidation and reduction reactivity of monoclinic WO_3 for solar energy conversion[J]. J Mater Chem, 2012, 22(14): 6746−6751.

[51] ZHANG M, ZHAO K, XIONG J, et al. A 1D/2D WO_3 nanostructure coupled with a nanoparticulate CuO cocatalyst for enhancing solar-driven CO_2 photoreduction: The impact of the crystal facet[J]. Sustain Energy Fuels, 2020, 4(5): 2593−2603.

[52] SHI W, GUO X, CUI C, et al. Controllable synthesis of Cu_2O decorated WO_3 nanosheets with dominant (001) facets for photocatalytic CO_2 reduction under visible-light irradiation[J]. Appl Catal B: Environ, 2019, 243: 236−242.

[53] IQBAL T, BILAL H, AFSHEEN S, et al. Investigation of sustainable Ag-WO_3 nanoparticles for environmental & photocatalytic remediation against methyl orange and its antimicrobial efficiency[J]. Mater Today Commun, 2025, 42: 111250.

[54] MAHANTA S K, SUMAN S, GHADEI S K, et al. Direct fabrication of metal-free graphene nanohairs/polyimide heterojunction for the highly efficient photocatalytic degradation of industrial dyes[J]. Diam Relat Mater, 2023, 137: 110096.

[55] ADHIKARI S, CHANDRA K S, KIM D H, et al. Understanding the morphological effects of WO_3 photocatalysts for the degradation of organic pollutants[J]. Adv Powder Technol, 2018, 29(7): 1591−1600.

[56] WANG X, FAN H, REN P. Effects of exposed facets on photocatalytic properties of WO_3[J]. Adv Powder Technol, 2017, 28(10): 2549−2555.

[57] ZHU Y, REN T, YUAN Z. Mesoporous phosphorus-doped g-C_3N_4 nanostructured flowers with superior photocatalytic hydrogen evolution performance[J]. ACS Appl Mater Interfaces, 2015, 7(30): 16850−16856.

[58] ZHANG D, WANG S, ZHU J, et al. WO_3 nanocrystals with tunable percentage of (001)-facet exposure[J]. Appl Catal B: Environ, 2012, 123−124: 398−404.

[59] WANG H, ZHANG G, XU Y, et al. Facile ethanol/water solvothermal synthesis of {001} facet oriented WO_3 architectures with superior simulated sunlight photocatalytic activities[J]. CrystEngComm, 2016, 18(41): 8089−8100.

[60] VORONTSOV A V, DUBOVITSKAYA V P. Selectivity of photocatalytic oxidation of gaseous ethanol over pure and modified TiO_2[J]. J Catal, 2004, 221(1): 102−109.

[61] DING J, CHAI Y, LIU Q, et al. Selective deposition of silver nanoparticles onto WO_3 nanorods with different facets: The correlation of facet-induced electron transport preference and photocatalytic activity[J]. J Phys Chem C, 2016, 120(8): 4345−4353.

[62] ZHU J, WANG S, XIE S, et al. Hexagonal single crystal growth of WO_3 nanorods along a [110] axis with enhanced adsorption capacity[J]. Chem Commun, 2011, 47(15): 4403−4405.

[63] SHEN F, HE S, TANG X. Breaking linear scaling relation

limitations on a dual-driven single-atom copper-tungsten oxide catalyst for ammonia synthesis[J]. Angew Chem Int Ed, 2025, 64(21): e202423154.

[64] LI J, LUO M, WANG M, et al. Electrocatalytic conversion of methane to ethanol by ultrathin WO_3 nanosheets: Oxygen vacancy engineering[J]. Appl Mater Today, 2023, 32: 101855.

[65] XU X, PAN L, ZHANG X, et al. Rational design and construction of cocatalysts for semiconductor-based photo-electrochemical oxygen evolution: A comprehensive review[J]. Adv Sci, 2019, 6(2): 1801505.

[66] YANG J, WANG D, HAN H, et al. Roles of cocatalysts in photocatalysis and photoelectrocatalysis[J]. Acc Chem Res, 2013, 46(8): 1900−1909.

[67] VILANOVA A, DIAS P, LOPES T, et al. The route for commercial photoelectrochemical water splitting: A review of large-area devices and key upscaling challenges[J]. Chem Soc Rev, 2024, 53(5): 2388−2434.

[68] JILANI A, IBRAHIM H. Development in photoelectrochemical water splitting using carbon-based materials: A path to sustainable hydrogen production[J]. Energies, 2025, 18(7): 1603.

[69] KUDO A, MISEKI Y. Heterogeneous photocatalyst materials for water splitting[J]. Chem Soc Rev, 2009, 38(1): 253−278.

[70] ZHAO Y, NIU Z, ZHAO J, et al. Recent advancements in photoelectrochemical water splitting for hydrogen production[J]. Electrochem Energy Rev, 2023, 6(1): 14.

[71] FUJISHIMA A, HONDA K. Electrochemical photolysis of water at a semiconductor electrode[J]. Nature, 1972, 238(5358): 37−38.

[72] ZHU T, CHONG M, CHAN E. Nanostructured tungsten trioxide thin films synthesized for photoelectrocatalytic water oxidation: A review[J]. ChemSusChem, 2014, 7(11): 2974−2997.

[73] MI Q, ZHANAIDAROVA A, BRUNSCHWIG B, et al. A quantitative assessment of the competition between water and anion oxidation at WO_3 photoanodes in acidic aqueous electrolytes[J]. Energy Environ Sci, 2012, 5(2): 5694−5700.

[74] WANG S, CHEN H, GAO G, et al. Synergistic crystal facet engineering and structural control of WO_3 films exhibiting unprecedented photoelectrochemical performance[J]. Nano Energy, 2016, 24: 94−102.

[75] LIU J, XU S, LI Y, et al. Facet engineering of WO_3 arrays toward highly efficient and stable photoelectrochemical hydrogen generation from natural seawater[J]. Appl Catal B: Environ, 2020, 264: 118540.

[76] Liu Y, WYGANT B, KAWASHIMA K, et al. Facet effect on the photoelectrochemical performance of a WO_3/$BiVO_4$ heterojunction photoanode[J]. Appl Catal B: Environ, 2019, 245: 227−239.

[77] SCHWACH P, PAN X, BAO X. Direct conversion of methane to value-added chemicals over heterogeneous catalysts: Challenges and prospects[J]. Chem Rev, 2017, 117(13): 8497−8520.

[78] SHIMURA K, KATO S, YOSHIDA T, et al. Photocatalytic steam reforming of methane over sodium tantalate[J]. J Phys Chem C, 2010, 114(8): 3493−3503.

[79] CHEN G, WATERHOUSE G I, SHI R, et al. Von sonnenlicht zu brennstoffen: Aktuelle fortschritte der C_1 - Solarchemie[J]. Angew Chem Int Ed, 2019, 131(49): 17690−17715.

[80] MA J, MAO K, LOW J, et al. Efficient photoelectrochemical conversion of methane into ethylene glycol by WO_3 nanobar arrays[J]. Angew Chem Int Ed, 2021, 60(17): 9357−9361.

[81] JIMENEZ-MORALES I, SANTAMARIA-GONZALEZ J, MAIRELES-TORRES P, et al. Zirconium doped MCM-41 supported WO_3 solid acid catalysts for the esterification of oleic acid with methanol[J]. Appl Catal A: Gen, 2010, 379(1−2): 61−68.

[82] ZHANG C, LIU T, WANG H, et al. Synthesis of acetyl salicylic acid over WO_3/ZrO_2 solid superacid catalyst[J]. Chem Eng J, 2011, 174(1): 236−241.

[83] MAITY N, BARMAN S, MINENKOV Y, et al. A silica-supported monoalkylated tungsten dioxo complex catalyst for olefin metathesis[J]. ACS Catalysis, 2018, 8(4): 2715−2729.

[84] HAMMOND C, STRAUS J, RIGHETTONI M, et al. Nanoparticulate tungsten oxide for catalytic epoxidations[J]. ACS Catalysis, 2013, 3(3): 321−327.

[85] JIANG W, HUANG R, LI P, et al. Metathesis and isomerization of n-butene and ethylene over WO_3/SiO_2 and MgO catalysts: Thermodynamic and experimental analysis[J]. Appl Catal A: Gen, 2016, 517: 227−235.

[86] GAO G, LV M, SHAO Y, et al. Crystal facet-dependent activity of h-WO_3 for selective conversion of furfuryl alcohol to ethyl levulinate[J]. Phys Chem Chem Phys, 2020, 22(46): 26923−26934.

[87] DONG C, ZHAO R, YAO L, et al. A review on WO_3 based gas sensors: Morphology control and enhanced sensing properties[J]. J Alloys Compd, 2020, 820: 153194.

[88] YAO M, LI Q, HOU G, et al. Dopant-controlled morphology evolution of WO_3 polyhedra synthesized by RF thermal plasma and their sensing properties[J]. ACS Appl Mater Interfaces, 2015, 7(4): 2856−2866.

[89] YIN M, YU L, LIU S. Synthesis of thickness-controlled cuboid WO_3 nanosheets and their exposed facets-dependent acetone sensing properties[J]. J Alloys Compd, 2017, 696: 490−497.

[90] WANG X, HAN W, YANG J, et al. Facet effect on diverse WO_3 morphologies and ideal work function for ppb-level triethylamine detection[J]. Sens Actuators B Chem, 2022, 363: 131849.

WO_3 在多相催化反应中的晶面效应

张　苗[1]，王会香[1,2,*]，李慧鹏[2,3]，张德顺[2,3]，徐静文[1]，任多佳[1]，
张　未[1]，薛首峰[1]，吕宝亮[1,2,*]

（1. 山西师范大学 化学与化工学院，山西 太原 030031；2. 煤基合成油产品测试厅市共建山西省重点实验室，山西 长治 046000；
3. 山西潞安煤基清洁能源有限责任公司，山西 长治 046200）

摘　要：WO_3 作为一种重要的过渡金属氧化物，凭借在环保性、成本控制及电学特性等方面的综合优势，已成为当前多相催化领域极具吸引力的核心催化材料之一。WO_3 不同晶面因原子排列方式、电子结构及表面能存在固有差异，因而在电荷分离效率、反应物吸附能力及氧化还原活性等关键催化物理化学性质上表现出显著区别。相关研究证实，受晶面效应影响，WO_3 催化性能强烈依赖于其几何形貌所决定的晶面暴露状态，这一发现为现代多相催化机理研究提供了重要方向。本工作综述了近年来 WO_3 作为多相催化剂，在光催化、电催化、光电催化以及热催化领域应用中的晶面效应；同时结合理论计算结果，从 WO_3 晶面的原子结构本质入手，阐释了晶面效应产生的内在机制。总结了 WO_3 在上述应用场景中晶面效应呈现的共性规律，探讨了当前 WO_3 晶面效应研究存在的不足，并对该领域未来的发展方向进行了展望。

关键词：WO_3；晶面效应；多相催化

中图分类号：O643.36　　**文献标识码：**A

作者简介：



张苗（1999 年），博士在读，研究方向为过渡金属氧化物结构调控及长链 α-烯烃的催化环氧化性能研究，zhangmiaosxnu@163.com。



吕宝亮（1983 年），博士研究生，教授，博士生导师，主要从事多相催化材料和先进功能材料的结构设计、合成及相关应用研究，lvbl@sxnu.edu.cn。



王会香（1986 年），博士研究生，副教授，硕士生导师，主要从事酸性过渡金属氧化物的结构调控及性能研究工作，wanghx@sxnu.edu.cn。